The influence of the impeller on carbonation performances in carbon capture using industrial by-products

International Journal of Thermofluids 29 (2025) 101385

Contents lists available at ScienceDirect

International Journal of Thermofluids

journal homepage: www.elsevier.com/locate/ijtf

The influence of the impeller on carbonation performances in carbon capture using industrial by-products

Abdul Raouf Tajik [a,b], Emmanouela Leventaki [c], Francisco Baena-Moreno [c], Christian Kugge [d], Diana Bernin [c], Henrik Ström [a], Gaetano Sardina [a,*]

[a] Division of Fluid Dynamics, Department of Mechanics and Maritime Sciences, Chalmers University of Technology, SE 412 96 Gothenburg, Sweden
[b] Fluids Engineering Department, Division of Mechanical Engineering, Southwest Research Institute, San Antonio, TX 78238, USA
[c] Department of Chemistry and Chemical Engineering, Chalmers University of Technology, SE 412 96 Gothenburg, Sweden
[d] Svenska Cellulosa Aktiebolaget SCA R&D Centre, Sidsjövägen 2, SE 851 21 Sundsvall, Sweden

ARTICLE INFO

Keywords:
Carbon Capture
Utilization and Storage (CCUS)
Carbonation process optimization
Computational Fluid Dynamics (CFD)
Gas–liquid mixing
Pitch blade impellers
Industrial by-products

ABSTRACT

This study investigates the performances of radial flow (Rushton turbine and Parabolic) and axial flow (Pitch Blade Down-pumping [PBD] and Pitch Blade Up-pumping [PBU]) impellers in promoting CO_2 capture via carbonation in various alkaline absorbents such as NaOH in ethanol, black liquor, and green liquor dregs. We performed experiments in a lab-scale reactor that show that the Rushton turbine exhibits superior effectiveness in industrial by-product-derived solutions such as 5% w/v aqueous green liquor dregs and black liquor, albeit at a high energy cost. However, in ethanol–NaOH mixtures, where the carbonation process inherently leads to an increase in viscosity, the PBD demonstrates superior efficiency. For example, in aqueous green liquor dregs at 400 rpm, down-pumping operation achieved pH = 8.5 with 13% improved performance at 25% w/v, whereas the up-pumping mode showed a 23% advantage at 5% w/v. In addition, power number reductions of up to 70% were observed with PBD compared to the Rushton impeller. Our main results are supported by numerical simulations that link impeller performances to mixing and vortical structures of the flow inside the reactor. The unique adaptability of the pitch blade, capable of mode-switching between down-pumping and up-pumping, offers distinct advantages through various stages of carbonation. The findings underscore the importance of analyzing the optimal impeller design for enhancing CO_2 absorption efficiently, considering operational factors and the inherent variations in the process, especially in view of designing a large-scale reactor.

1. Introduction

Carbon capture and storage (CCS) and carbon capture and utilization (CCU) are two approaches aimed at reducing CO_2 emissions and limiting the effects of climate change. CCS involves collecting CO_2 from industrial processes [1] and storing it underground to prevent its release into the atmosphere [2–4]. CCU, in contrast, converts captured CO_2 into materials that can be used in different industrial sectors. Carbonation using alkaline absorbents is one CCU method. It allows the formation of carbonates, which can be either unstable or stable depending on the absorbent. Unstable carbonates can be treated with weak acids to release pure CO_2, which can then be stored or reused [5]. Stable carbonates can be used in construction, agriculture, and other applications [6].

Several studies have investigated the use of industrial alkaline residues as CO_2 absorbents [7–12]. These include steelmaking slag, fly ash, and green liquor dregs, which contain metal oxides that react with CO_2 to form solid carbonates. Using these residues may reduce the need for raw materials and also support their reuse in various sectors. For example, the resulting carbonated materials can be used in the production of alternative construction materials [13].

Process development still faces technical challenges such as improving the efficiency of CO_2 capture and designing systems that are practical for industrial use. Understanding the influence of mixing and reactor design is crucial for the development of novel systems.

* Corresponding author.
E-mail addresses: raouf.tajik@swri.org (A.R. Tajik), sardina@chalmers.se (G. Sardina).

https://doi.org/10.1016/j.ijft.2025.101385
Received 22 March 2025; Received in revised form 8 August 2025; Accepted 15 August 2025
Available online 22 August 2025

Nomenclature

Symbols

θ	Azimutal coordinate (m)
C_D	Drag coefficient (–)
d_B	Bubble diameter (m)
D_{reactor}	Reactor diameter (m)
D_{AB}	Diffusion coefficient in ($m^2\,s^{-1}$)
Eo	Eötvös number (–)
g	Acceleration of gravity ($m\,s^{-2}$)
k	Turbulent kinetic energy ($m\,s^{-}$)
Mo	Morton number (–)
p	Static pressure (Pa)
P_{req}	Power for impeller rotation (W)
Q	Q-criterion (s^{-2})
r	Radial coordinate (m)
r_{blade}	Blade radius (m)
Re_B	Bubble Reynolds number (–)
S	Strain rate tensor, (s^{-1})
Sh	Sherwood number (–)
S_k^{BIT}	Bubble-induced-turbulance source in $k-$equation ($N\,m^{-2}\,s^{-2}$)
S_ϵ^{BIT}	Bubble-induced-turbulance source in $\epsilon-$equation, ($N\,m^{-2}\,s^{-2}$)
Sc	Schmidt number (–)
u, $\mathbf{u}$	Resolved velocity, ($m\,s^{-1}$)
u', $\mathbf{u}'$	Fluctuating velocity, ($m\,s^{-1}$)
u_{rel}, $\mathbf{u}_{rel}$	Relative velocity between phases, ($m\,s^{-1}$)
z	Axial coordinate (m)

Greek symbols

α	Volume fraction, (–)
Δ	Grid scale in IDDES model (m)
ϵ	Turbulent dissipation rate, ($m^2\,s^{-3}$)
μ	Dynamic viscosity (Pa s)
ν	Kinematic viscosity ($m^2\,s^{-1}$)
Ω	Vorticity (s^{-1})
ω	Turbulence dissipation rate (s^{-1})
ω_{blade}	Impeller rotation speed, (rpm)
ρ	Density ($kg\,m^{-3}$)
σ	Surface tension coefficient ($N\,m^{-1}$)
τ_k	Laminar stress tensor ($N\,m^{-2}$)
τ_k^{Re}	Turbulent stress tensor ($N\,m^{-2}$)

Computational Fluid Dynamics (CFD) is often used to support this understanding. CFD has been applied to analyze CO_2 adsorption processes [14], mixing performance [15], bubbly flows [16], and other fluid-based systems [17,18]. CFD has also been used in carbonation research to evaluate fluid flow, predict kinetics, and study reactor behavior [19–22].

Most existing carbonation studies have focused on bubble column reactors or stirred systems without detailed analysis of the mixing components. Limited work has investigated the specific use of impellers in carbonation processes, and studies addressing the influence of impeller design on gas–liquid flow and CO_2 transfer in systems using industrial by-products are especially scarce. This study aims to address this gap by evaluating how different impeller types affect the hydrodynamics and carbonation efficiency in such systems.

This study uses both CFD simulation and laboratory experiments to evaluate how impeller geometry and speed affect mixing and carbonation. We studied four impeller configurations, including Rushton, parabolic, pitch blade up-pumping (PBU), and pitch blade down-pumping (PBD) designs. These impellers were selected to represent both radial-flow (Rushton and parabolic) and axial-flow (pitched-blade) behaviors. Radial-flow impellers are often used for gas–liquid dispersion due to their shear and vortex characteristics, while axial-flow impellers are better suited for maintaining flow uniformity, especially in systems where the viscosity changes during operation. The selected designs are also practical for simulation and scale-up. The systems studied include black liquor, 5% and 25% w/v green liquor dregs in water, and ethanol solutions with 2 g/L and 10 g/L NaOH. pH measurements are used to monitor the effect of gas–liquid mixing on CO_2 absorption. The goal is to provide information on how impeller design affects carbonation dynamics in systems using industrial residues. This study does not aim to perform detailed chemical reaction modeling but rather focuses on linking hydrodynamics, mass transfer, and carbonation performance through combined experiments and CFD simulations.

2. Experiments

2.1. Absorption systems

Three absorption systems were considered for carbon dioxide capture: black liquor, green liquor dregs, and solutions of NaOH in ethanol in two different concentrations. In all systems, the absorption of carbon dioxide is primarily chemical via reactions of carbonation between the gaseous carbon dioxide and the metal ions in the liquid medium. Nevertheless, the different liquids have widely different physicochemical properties, making them interesting candidates for studying the effect of impeller design on their carbon capture performance.

Black liquor is a by-product of the pulp and paper industry [23]. It is generated from the treatment of lignocellulosic biomass for pulp production. Several chemical and mechanical processes can be used to separate the lignin and hemicelluloses from the cellulose. The preferred method for biomass coming from non-woody sources, such as wheat and oat husks, is soda pulping [24]. This process consists of chemical treatment of the biomass with aqueous solutions of NaOH, which breaks down the lignocellulosic structure. The by-product of this process is an alkaline liquid high in lignin, hemicellulose, NaOH, and other organic and inorganic compounds [24]. Due to its high alkalinity, black liquor can absorb carbon dioxide via inorganic carbonation with NaOH towards the formation of sodium carbonate and bicarbonate following reactions [25]. Since these minerals are soluble in aqueous systems, they reside in black liquor in the form of sodium cations and carbonate or bicarbonate anions:

$$2\,NaOH_{(aq)} + CO_{2(g)} \rightleftharpoons Na_2CO_{3(aq)} + H_2O_{(l)} \quad \text{(R1)}$$

$$2\,NaOH_{(aq)} + CO_{2(g)} \rightleftharpoons NaHCO_{3(aq)} \quad \text{(R2)}$$

$$Na_2CO_{3(aq)} + CO_{2(g)} + H_2O_{(l)} \rightleftharpoons 2\,NaHCO_{3(aq)} \quad \text{(R3)}$$

Green liquor dregs (GLD) are a residue also coming from the same industry. Industrially, wood is the main biomass for pulp production. The most popular process for the extraction of cellulose from wood is Kraft pulping, which uses a solution of NaOH and sodium sulfide [23]. The generated black liquor is then transferred to the recovery boiler, where it is burned for energy production. After the recovery boiler, green liquor and GLD remain. The green liquor is further treated to recover pure cooking liquor, which is recycled back into the process, but the GLD is a waste, and it is disposed of in the landfill [26]. Fig. 1 shows a diagram of the overall process.

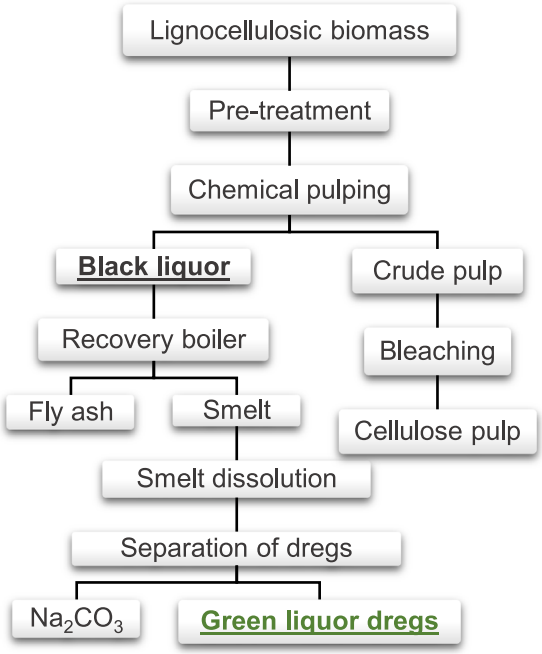

Fig. 1. Simplified scheme of a typical industrial pulp and paper process from the raw material until the separation of green liquor dregs, modified from [26,27]. (For interpretation of the references to color in this figure legend, the reader is referred to the web version of this article.)

GLD typically contains high amounts of calcium oxide and other metal oxides, such as magnesium, sodium, potassium, etc., at varying concentrations [28]. Research on the utilization of GLD is limited, with most studies focusing on its use as a sealant to cover mines for preventing acid mine drainage [29,30]. More recently, this residual stream has also been investigated for carbon dioxide capture, notably in a study by Queiroz et al. [31], which employed a bubble column reactor rather than a stirred tank. Given GLD's richness in metal oxides, it was deemed relevant to include it in the present study as well. The reaction between carbon dioxide and the metal oxides available in GLD leads to the formation of inorganic carbonates. Calcium and magnesium carbonates are insoluble in water and precipitate as they form, while potassium and sodium carbonates are soluble. The chemical equations of carbonation with calcium and magnesium oxides are presented below [32,33]:

$$CaO_{(s)} + H_2O_{(l)} \longrightarrow Ca(OH)_{2(aq)} \quad \text{(R4)}$$

$$Ca(OH)_{2(aq)} + CO_{2(g)} \longrightarrow CaCO_{3(s)} + H_2O_{(l)} \quad \text{(R5)}$$

$$MgO_{(s)} + H_2O_{(l)} \longrightarrow Mg(OH)_{2(aq)} \quad \text{(R6)}$$

$$Mg(OH)_{2(aq)} + CO_{2(g)} \longrightarrow MgCO_{3(s)} + H_2O_{(l)} \quad \text{(R7)}$$

Solutions of sodium and potassium hydroxide in methanol and ethanol have previously been investigated for their CO_2 absorption capacity [5,34–36]. For instance, Baena-Moreno et al. [5] examined the absorption of CO_2 in ethanol-based NaOH solutions at concentrations between 2 g/L and 10 g/L. During those experiments, a gel was observed to form, which hindered effective gas–liquid mixing. The exact cause of this gel formation remains unclear. According to the literature, the absorption mechanism involves both organic and inorganic carbonation pathways, as illustrated in the following reactions [5,34]:

$$C_2H_5OH_{(l)} + NaOH_{(aq)} + CO_{2(g)} \rightleftharpoons C_2H_5OCOONa_{(s)} + H_2O_{(l)} \quad \text{(R8)}$$

$$C_2H_5OH_{(l)} + NaOH_{(aq)} + CO_{2(g)} \rightleftharpoons C_2H_5OH_{(l)} + NaHCO_{3(aq)} \quad \text{(R9)}$$

Table 1
Composition of the GLD obtained from Svenska Cellulosa AB.

Compound	Percentage in total solids
Silicon dioxide	1.86
Aluminium oxide	0.918
Calcium oxide	25.0
Iron(III) oxide	0.435
Potassium oxide	0.199
Magnesium oxide	12.5
Manganese(II) oxide	2.44
Sodium oxide	3.76
Phosphorus pentoxide	0.532
TiO_2	0.0233

2.2. Methodology

The black liquor was prepared from cooking oat husks with the soda pulping method, according to Leventaki et al. [37]. 2.6% w/v of a commercial antifoaming agent (BIM Kemi) was added to reduce the foaming of the liquor. A sample of GLD was provided by the company SCA (Svenska Cellulosa AB). The composition of the material is given in Table 1. Aqueous mixtures of GLD were prepared by adding GLD in water at concentrations of 5% w/v and 25% w/v and stirring them for 24 h.

Finally, solutions of NaOH in ethanol were prepared by dissolving NaOH (97.0%–100% w/v, VWR Chemicals) in a mixture of 96% ethanol and 4% deionized water at concentrations of 2 g/L and 10 g/L. As shown in Fig. 2, all experiments were conducted at ambient pressure and temperature in a plastic container (150 mL, VWR) configured as a gas–liquid stirred tank reactor. The gas phase consisted of 15% CO_2 and 85% N_2, representative of flue gas compositions. he gas was sparged into the liquid phase at a flow rate of 200 mL/min using a DURAN glass frit sparger with a diameter of approximately 12 mm. The working liquid volume was fixed at 100 mL. This setup corresponds to a superficial gas velocity of approximately 0.03 m/s, which was also used as an input boundary condition in the CFD simulations. A mechanical stirrer (EUROSTAR Power Control-Visc, IKA®) was used to mix the solutions with four different impeller types, each 3D-printed via stereolithography (Form 3+, Formlabs) following established additive manufacturing methods [38,39]. Carbonation progress was monitored using a pH meter (HQ430D, HACH). For each absorbent system, a pH limit was defined and the time required to reach this value was recorded to compare impeller performance. The pH meter was calibrated using aqueous standard solutions; for ethanol-based solvents, pH is expressed as pH_S, as defined by IUPAC [40]. Although the initial pH of NaOH–ethanol solutions exceeded 14, the corresponding electrode voltage was consistent with that of aqueous systems at pH 14, allowing for valid relative comparisons during carbonation despite the limitations of pH measurement in non-aqueous media.

During the experiments, it was noticeable that the viscosity and surface tension of the absorbents significantly affected the bubble sizes and the flow field. Both black liquor and ethanol-NaOH formed foam at the surface of the liquid during the gas sparging. In addition, the ethanol-NaOH solutions tend to form a gel during the absorption of carbon dioxide, as mentioned earlier. To better understand the effect of these phenomena and represent it more accurately with CFD simulation, the viscosity and surface tension of the absorbents were measured using a

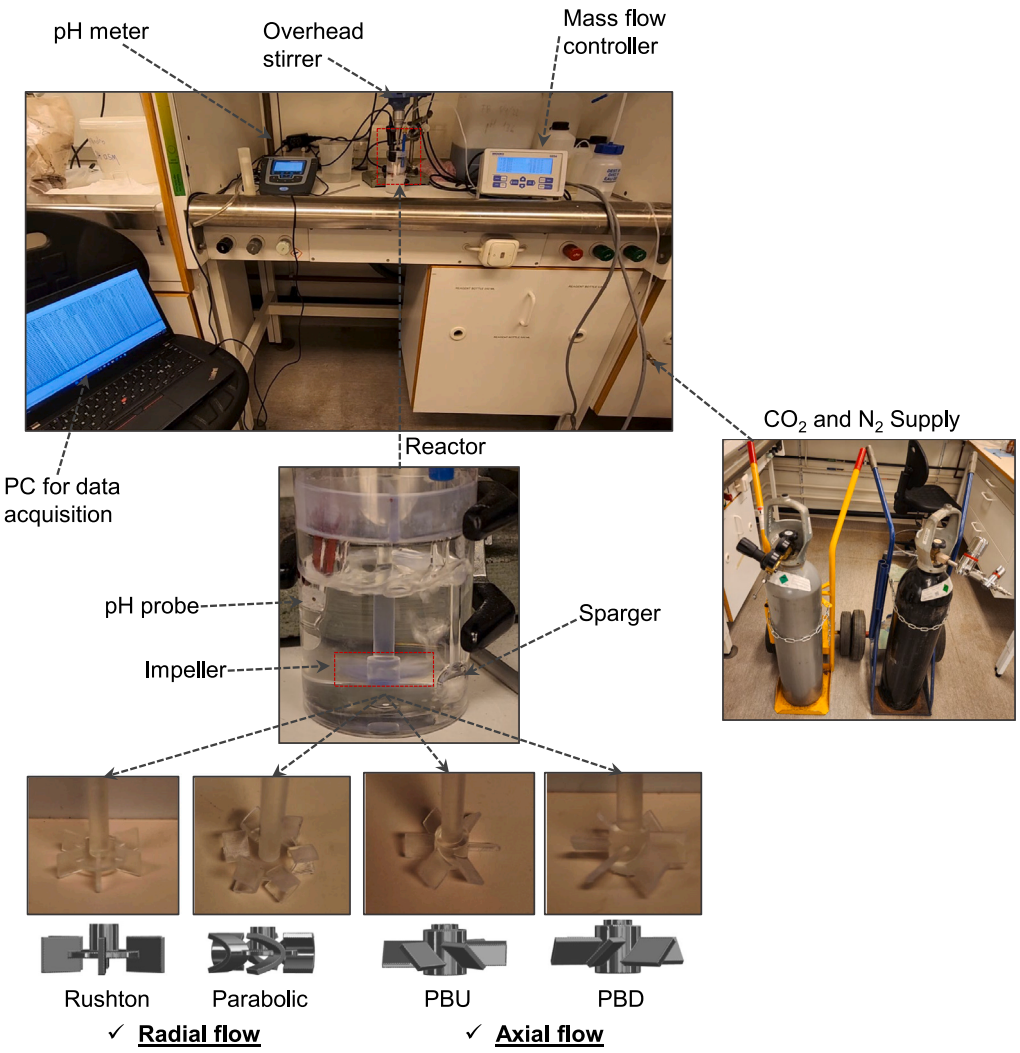

Fig. 2. Experimental setup for carbonation, featuring a controlled supply of CO_2 and N_2 gases, integrated data acquisition through a dedicated PC, and precision pH metering. The system employs the Brooks 0250 series set-point controller. The reactor is equipped with a sparger, and the stirring mechanism is governed by an overhead stirrer. Four distinct 3D-printed impeller designs are also showcased.

Table 2
Measured physicochemical properties of water and four different solutions post-carbonation.

	Water	Black liquor	GLD (5% w/v)	GLD (25% w/v)	Ethanol-NaOH (2g/L)	Ethanol-NaOH (10g/L)
Density, ρ ($kg\,m^{-3}$)	990	1045	1014	1075	808	794
Viscosity, μ (mPa s)	1.003	2.82	1.32	5.16	2.4	14.2
Surface tension, σ ($mN\,m^{-1}$)	72.5	32.7	73.2	77.1	24.3	23.2
pH	7.0	10.0	7.2	7.2	9.0	9.8

Digital DV-I+ Viscometer (Brookfield) and an Attention Theta optical tensiometer (Biolin Scientific), respectively.

The carbonation process influenced the physical properties of each absorbent system to varying degrees. In the case of GLD, changes were minor and primarily governed by the solids-to-water ratio. The formation of solid $CaCO_3$ and soluble Na_2CO_3 did not significantly affect viscosity or surface tension. The ethanol–NaOH systems, however, underwent notable changes, forming a gel-like suspension during carbonation. These changes were evident visually and confirmed by physical property measurements. As shown in Table 2, the viscosity of the 2 g/L NaOH solution increased from ethanol's baseline value of 1.18 mPa s [41] to 2.4 mPa s, and rose sharply to 14.2 mPa s for the 10 g/L solution, while surface tension remained close to ethanol's reference of 22 $mN\,m^{-1}$. The post-carbonation pH of these ethanol-based systems also dropped from highly alkaline values, indicating the consumption of NaOH during CO_2 absorption. Black liquor showed minimal physical change at high pH (10.0) and is known to undergo precipitation of lignin and silica only below pH 10 [37], which was not the case in this study.

3. Governing equations and numerical methodology

In the context of multiphase flow simulations, particularly for systems with diverse design and operating conditions, computational efficiency becomes paramount. We have therefore adopted the Unsteady Reynolds-Averaged Navier–Stokes (URANS) approach, which provides a balance between computational efficiency and fidelity. Coupled with the Eulerian multiphase model, URANS becomes especially potent for simulating dispersed multiphase flows, such as gas sparging into liquids. The multifluid Eulerian–Eulerian model, treating the phases as interpenetrating continua, accurately captures the interactions between the gas and liquid phases [42,43].

However, we acknowledge that this modeling framework does not resolve bubble coalescence and breakup dynamics directly. For more detailed characterization of bubble size distributions and local interfacial phenomena, advanced approaches such as population balance modeling (PBM) or interface-resolving methods (e.g., VOF or front-tracking) would be required. These models, while more computationally intensive, offer improved fidelity for systems where bubble evolution plays a dominant role in mass transfer. Future work may incorporate such techniques to enhance the predictive accuracy of the simulation results.

3.1. Multiphase Eulerian framework

The phasic continuity equations for bubbly flow reads:

$$\frac{\partial}{\partial t}\left(\alpha_k \rho_k\right) + \nabla \cdot \left(\alpha_k \rho_k \mathbf{u}_k\right) = 0 \tag{1}$$

While the phasic momentum equations in the Eulerian-Eulerian model are expressed as follows:

$$\frac{\partial}{\partial t}\left(\alpha_k \rho_k \mathbf{u}_k\right) + \nabla \cdot \left(\alpha_k \rho_k \mathbf{u}_k \otimes \mathbf{u}_k\right) = -\alpha_k \nabla p + \nabla \cdot \left(\alpha_k \left(\boldsymbol{\tau}_k + \boldsymbol{\tau}_k^{Re}\right)\right) + \mathbf{F}_k^{body} + \mathbf{F}_k^{inter} \tag{2}$$

In the above equations, p is the pressure common to both phases, and $\mathbf{u}_k$, α_k, and ρ_k are the velocity, volume fraction, and density of phase k, respectively. In the following, we will use the indices L and G to denote continuous liquid and dispersed gas. Indices i and j denote Cartesian coordinates. τ_k and τ_k^{Re} the laminar and turbulent stress tensors, respectively. The body forces $\mathbf{F}_k^{body}$ that need to be considered in the present work are the gravity force as well as centrifugal and Coriolis forces where a rotating frame of reference is used. An additional term $\mathbf{F}_k^{inter}$ appears in Eq. (2) that signifies the momentum transfer between phases. For momentum exchange between liquid and gas phases, multiple forces can be considered, such as drag, virtual mass, lift, wall, and turbulent dispersion. However, in a mechanically stirred reactor, only the drag force in the interphase momentum exchange term $\mathbf{F}^{drag}$ is considered significant [44–47]. This drag force counteracts the relative bubble motion in the surrounding liquid. The momentum source for the gas phase due to this drag force is:

$$\mathbf{F}^{drag} = \frac{3}{4}\frac{C_D}{d_B}\alpha_G \rho_L |\mathbf{u}_{rel}| \mathbf{u}_{rel} \tag{3}$$

The drag coefficient C_D is largely dependent on the bubble Reynolds number $Re_B = \frac{|\mathbf{u_{rel}}| d_B}{\nu_L}$. For deformable bubbles, it also depends on the Eötvös number $Eo = \frac{g \Delta\rho d_B^2}{\sigma}$, but is independent of the Morton number $Mo = \frac{g \Delta\rho \rho_L^2 \nu_L^4}{\sigma^3}$. A correlation distinguishing different bubble-shape regimes was proposed by Ishii and Zuber [48]:

$$C_D = max(C_{D,sphere}, min(C_{D,ellipse}, C_{D,cap})) \tag{4}$$

where

$$\begin{cases} C_{D,sphere} = \frac{24}{Re}(1 + 0.15 Re_B^{0.75}) \\ C_{D,ellipse} = \frac{2}{3}\sqrt{Eo} \\ C_{D,cap} = \frac{8}{3} \end{cases} \tag{5}$$

This correlation aligns well with a broad dataset on bubble terminal velocity in stationary liquids, spanning several magnitudes of Re, Eo, and Mo [49].

3.2. Turbulence modeling

To solve the momentum equation, the turbulent stress tensor τ_k^{Re} needs to be obtained from a turbulence model. Turbulence in the continuous phase is modeled with a multiphase formulation of the standard $k-\epsilon$ turbulence model [50]. In this context, k_L and ϵ_L denote the turbulent kinetic energy and the dissipation rate within the liquid phase, respectively:

$$\frac{\partial}{\partial t}\left(\alpha_c \rho_L k_L\right) + \nabla \cdot \left(\alpha_L \rho_L \mathbf{u}_L k_L\right) = \nabla \cdot \left(\alpha_L \left(\mu_L + \frac{\mu_{t,L}}{\sigma_k}\right)\nabla k_L\right) + \alpha_L \left(P_{k,c} - \rho_L \epsilon_L\right) + \alpha_L S_k^{BIT} \tag{6}$$

$$\frac{\partial}{\partial t}\left(\alpha_c \rho_L \epsilon_L\right) + \nabla \cdot \left(\alpha_L \rho_L \mathbf{u}_L \epsilon_L\right) = \nabla \cdot \left(\alpha_L \left(\mu_L + \frac{\mu_{t,L}}{\sigma_\epsilon}\right)\nabla \epsilon_L\right) + \alpha_L \frac{\epsilon_L}{k_L}\left(C_{\epsilon,1} P_{k,c} - C_{\epsilon,2} \rho_L \epsilon_L\right) + \alpha_L S_\epsilon^{BIT} \tag{7}$$

It is seen that all single-phase terms are simply multiplied by the liquid volume fraction, whence it is assumed that the coefficients retain their single-phase values. Source terms S_k^{BIT} and S_ϵ^{BIT} describing the effects of the dispersed phase appear additively. It is important to note that both our experimental and numerical vessels were unbaffled. It is well-established that baffling significantly influences mixing dynamics and turbulence structures within stirred vessels [51]. While acknowledging that two-equation turbulence models typically have limitations in unbaffled stirred tanks due to high curvature and strong streamline curvature effects in rotating flows, the relatively low Reynolds number conditions explored here justify their application, providing a balance between computational accuracy and efficiency (see, e.g., [52–54]) for two-phase and [55] for single-phase reactors.

- **Source term for bubble-induced turbulence:**

Bubble-induced turbulence (BIT) is crucial for analyzing bubbly flows. BIT results from interactions between dispersed gas bubbles and the continuous liquid flow. The bubble motion and wake dynamics can significantly modify the turbulence properties, influencing transport characteristics like mixing, heat, and mass transfer. Hence, accurate bubbly flow simulations or analyses should account for BIT effects. One method represents BIT in models as an effective viscosity, factoring in the additional turbulence due to bubble interactions. A more detailed approach directly adds source terms in the turbulence equations to capture bubble-flow interactions. Among these, the Troshko and Hassan model [56] integrates source terms for precise bubbly flow depiction. The source term S^k in the k-equation, given the work due to drag forces [56,57], is:

$$S_k^{BIT} = C_k^{BIT} \mathbf{F}^{drag} \cdot \mathbf{u}_{rel} \tag{8}$$

where $C_k^{BIT} = 0.75$. The source term S_ϵ^{BIT} in the ϵ-equation is derived by dividing the k-source by the time scale τ^{BIT}:

$$S_\epsilon^{BIT} = C_\epsilon^{BIT} \frac{S_k^{BIT}}{\tau^{BIT}} \tag{9}$$

where $\tau^{BIT} = \frac{d_B}{3 C_D |u_{rel}|}$ is a time scale.

3.3. Hybrid RANS/LES modeling of liquid phase

Building upon the governing equations presented in the preceding section, where the URANS Eulerian approach was employed for the two-phase flow, this section pivots to focus solely on the liquid phase dynamics. Given the reduced computational demands of single-phase analysis, we also exploit the capabilities of the Detached Eddy Simulation (DES) for a more detailed understanding. The DES, a hybrid computational fluid dynamics model, seamlessly blends the merits of both Reynolds-Averaged Navier–Stokes (RANS) and Large Eddy Simulation (LES) methodologies. This union ensures a detailed capture of the liquid phase responses, particularly when considering the influence of various impeller designs within our mixing tank setup. In regions defined by prominent, unsteady turbulence — often found trailing impellers or adjacent to the liquid surface — DES operates in an LES-like mode, directly resolving these primary turbulent structures.

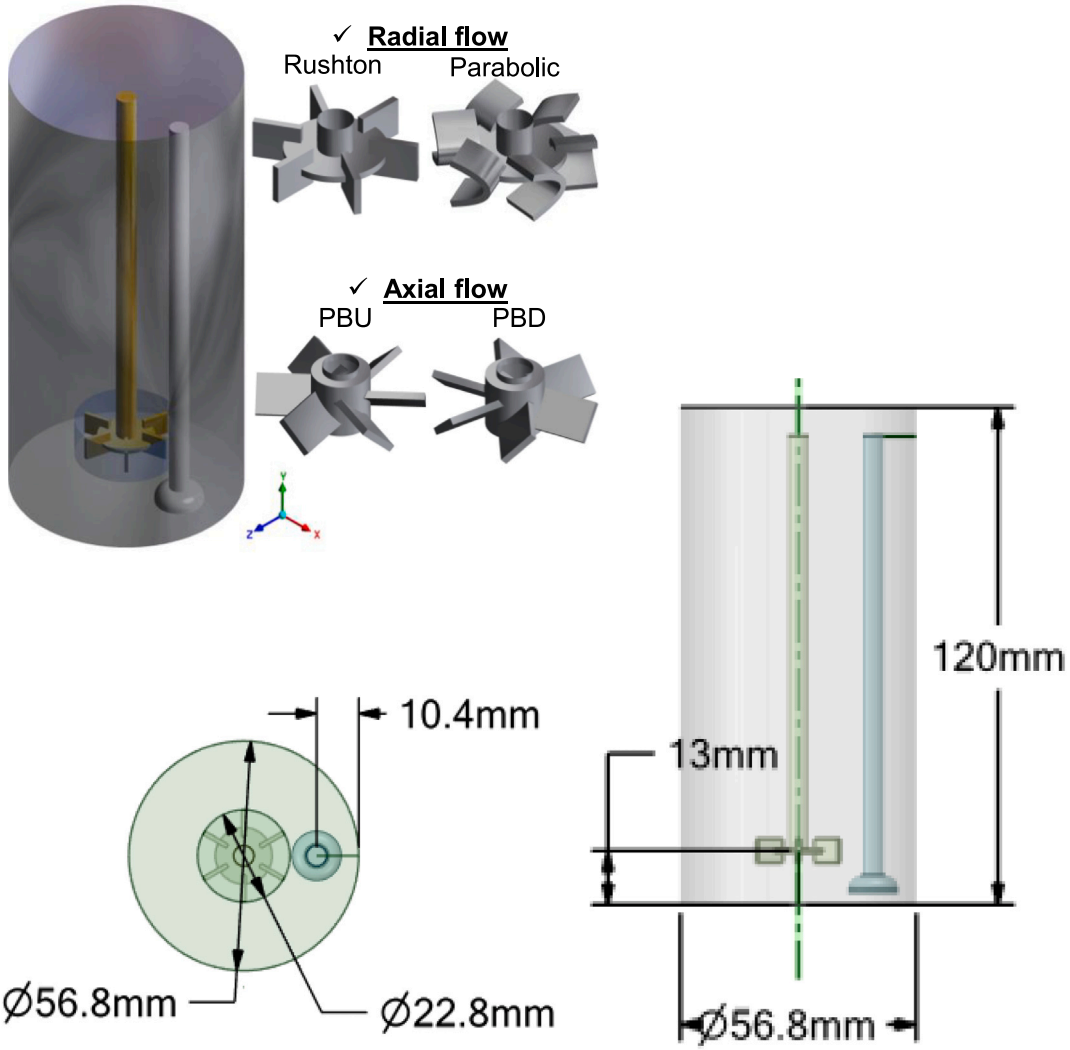

Fig. 3. Schematic representation of the mixing tank system. The left side shows the reactor setup with impeller and sparger; the right side illustrates four impeller designs: Rushton and Parabolic (radial flow), and Pitch Blade Up Pumping (PBU) and Pitch Blade Down Pumping (PBD) (axial flow). Dimensional annotations are provided for the Rushton turbine as a representative example, and apply similarly to the other impellers.

However, in areas dominated by finer, near-wall turbulence, DES takes on a RANS approach, modeling these disturbances rather than resolving them in their entirety.

In this study, the Improved Delayed Detached Eddy Simulation (IDDES)-SST approach is employed. The IDDES model incorporates a delay factor to enhance the model's differentiation between LES and RANS areas on the grid. This is crucial when mesh refinement creates overlapping zones. Consequently, RANS is employed in the slimmer near-wall area, where wall spacing is notably smaller than the boundary layer thickness. Stemming from DDES, IDDES was introduced to offer enhanced WMLES (Wall-modeled LES) capabilities compared to DES and DDES models [58,59]. In the IDDES formulation, two auxiliary functions are added for computing the revised wall distance to infuse WMLES competencies: the blending function f_B and the so-called "elevating" function f_e, making IDDES particularly suitable for our mixing tank setup with complex impeller geometries and flow interactions. Modification is required in the dissipation-rate term of the turbulent kinetic energy (TKE) transport equation:

$$\frac{\partial(\rho k)}{\partial t} + \nabla \cdot (\rho \mathbf{u} k) = \nabla \cdot \left((\mu + \mu_t \sigma_k)\nabla k\right) + \tau_{ij} S_{ij} - \frac{\rho\sqrt{k^3}}{l_{RANS} \text{ or } l_{IDDES}} \quad (10)$$

For RANS simulations, the turbulence length scale is given by $l_{\text{RANS}} = \frac{k^{1/2}}{\beta^* \omega}$, where $\beta^* = 0.09$ is the coefficient in the SST $k-\omega$ model. In the IDDES simulations, l_{RANS} is transformed into $l_{\text{HYBRID}} = \frac{k^{1/2}}{f_{\beta^*}\beta^*\tilde{\omega}}$ with f_{β^*} acting as the free-shear modification factor.

$$l_{\text{IDDES}} = f_d(1+f_e)l_{\text{RANS}} + (1-f_d)l_{\text{LES}} = f_d(1+f_e)l_{\text{RANS}} + (1-f_d)C_{\text{DES}}\Delta_{\text{IDDES}} \quad (11)$$

The grid scale Δ_{IDDES} is defined as:

$$\Delta_{\text{IDDES}} = \min\left(\max(0.15d_w, 0.15\Delta, \Delta_{\min}), \Delta\right) \quad (12)$$

where C_{DES} is a model constant for the DES model, d_w is the distance to the wall, Δ is the grid scale, and $\Delta_{\min}$ is the smallest distance between the cell center under consideration and the cell centers of the neighboring cells. The methodology follows the comprehensive framework established by Shur et al. [60] and Gritskevich et al. [61].

3.4. Details of the numerical solution

The model was solved with ANSYS FLUENT (Version 2022 R2) based on a control-volume approach. To accurately capture the rotational effects of the impeller within the vessel, a sliding-grid technique was employed. Though the Multiple Reference Frame (MRF) method is commonly used for simulating rotating machinery, in this study, the sliding-grid technique was preferred due to its ability to provide a

Table 3
Geometric parameters of the mixing tank setup.

Parameter	Relative to D_{reactor}	Absolute value (mm)
Tank diameter, D_{reactor}	1.000	56.8
Impeller diameter, d_{blade}	0.400	22.72
Impeller clearance from bottom	0.228	13.0
Sparger clearance from bottom	0.183	10.4
Liquid height	–	45.0

more accurate representation of the transient and dynamic interactions between the rotating impeller and the surrounding fluid. At the sparger inlet, the velocity of the liquid phase was maintained at zero, whereas the superficial gas velocity was determined to be $u_{GS} = 29.47\,\text{mm s}^{-1}$ with a gas volume fraction $\alpha_G = 1.0$. We used the experimental correlation provided by Kazakis et al. [62] to calculate the mean bubble diameter (d_B). Kazakis et al. investigated the effects of liquid properties and sparger pore size on the initial bubble size distribution in bubble columns, formulating a correlation for predicting the initial mean Sauter diameter of bubbles emanating from porous spargers in a homogeneous regime. For our study, applying this correlation yields a mean bubble diameter of 4.2 mm for water and 3.0 mm for ethanol, highlighting the variation in d_B dependent on the liquid utilized and emphasizing the significant role played by phenomena occurring at the sparger surface during bubble formation. The correlation serves as a practical estimation method for setting a representative bubble size in our CFD simulations, consistent with the operating conditions and liquid properties used in this study.

No-slip boundary conditions were applied to all vessel walls, shafts, impellers, and sparger surfaces, while a degassing boundary condition was applied at the reactor's top, allowing only the gas phase to escape. For the coupling of velocity and pressure, the SIMPLE algorithm was chosen. The momentum and turbulence equations were discretized using a first-order upwind scheme, while the QUICK (Quadratic Upstream Interpolation for Convective Kinematics) method was employed for the volume fraction equation. The bounded second-order implicit method managed the transient nature of the simulations. To ensure the accuracy and reliability of the solution, the convergence criterion was stringently set to 10^{-4} for all residuals of the transport equations. An adaptive time step was employed, guaranteeing the global CFL (Courant–Friedrichs–Lewy) number consistently remained below unity.

Table 3 summarizes the key geometric parameters of the mixing tank system used in this study, which includes both an impeller and a sparger, reflecting typical features of industrial mixing setups. The tank had a diameter $D_{\text{reactor}} = 56.8\,\text{mm}$, and the impeller diameter d_{blade} was set to 40% of that value. Clearances of both the impeller and sparger from the tank bottom were selected based on standard design practices. The total liquid height during experiments was 45 mm, corresponding to 100 mL of fluid. This value was confirmed experimentally to account for the volume displaced by internal components. It is also important to note that the pH probe was not included in the CFD geometry. The probe was located near the tank wall, well outside the impeller's main flow region. As a result, its influence on the bulk fluid dynamics was considered negligible, and it was omitted to simplify the computational domain.

Fig. 3 also presents the four impeller configurations analyzed in this study: the Rushton and Parabolic designs, which are classified as radial flow impellers, and the Pitch Blade Up Pumping (PBU) and Pitch Blade Down Pumping (PBD) designs, which generate axial flow. The rationale for selecting these impeller types extends beyond their flow characteristics and typical applications; it also includes the need to evaluate their torque behavior and power consumption. Notably, the Rushton impeller is known for producing high shear, which generally correlates with increased torque relative to the other designs. Radial impellers like the Rushton and Parabolic are particularly effective for gas dispersion and solid suspension, whereas axial impellers such as

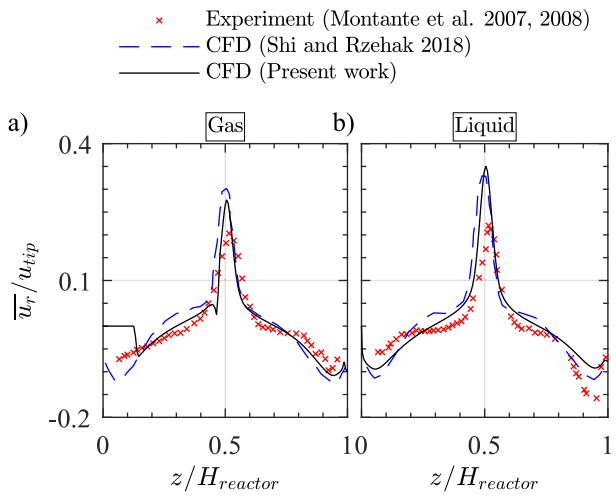

Fig. 4. Axial profiles of time-averaged radial velocities normalized by the Rushton impeller tip velocity $\frac{\overline{u_r}}{u_{tip}}$: (a) for the gas phase and (b) for the liquid phase. Data are taken at an impeller rotational speed of $\omega_{\text{blade}} = 450$ rpm and at a radial distance defined by $\frac{2r_{blade}}{D_{reactor}} = 0.85$.

PBU and PBD are preferred for promoting uniform blending in larger reactor volumes.

Dimensional details for all impeller designs, including the Rushton turbine, Parabolic, Pitch Blade Up-pumping (PBU), and Pitch Blade Down-pumping (PBD), are provided in Table 4. In industrial applications, the selection of the impeller type is typically guided by a techno-economic balance between the desired level of mixing and the associated energy consumption.

3.5. Numerical validation

For accurate fluid dynamics modeling, it is important to validate computational results against reliable experimental and previously published computational data. In our current study, we compare the axial profiles of time-averaged radial velocities, normalized by the impeller tip velocity, throughout the tank height. Fig. 4 distinctly showcases that our computational outcomes align closely with the experimental findings by Montante et al. [53,63] and the CFD results reported by Shi and Rzehak [54]. By examining both gas and liquid phase profiles, captured at an impeller rotational speed of $\omega_{\text{blade}} = 450$ rpm and a radial distance $\frac{2r_{blade}}{D_{reactor}} = 0.85$, we underline the precision and reliability of our methodology when compared with these previous studies. It should be noted that for validation purposes (Fig. 4), our CFD simulations were conducted using a baffled tank geometry, consistent with the experimental setup reported in [53,63]. This case was selected because it provides a well-documented SPIV dataset with high-resolution velocity field measurements suitable for benchmarking CFD solvers. Although baffling affects the flow characteristics, the purpose of this validation was to ensure that the overall CFD methodology, including meshing strategy, turbulence model, and multiphase setup, was correctly implemented. All subsequent simulations in this study were performed using an unbaffled tank geometry to match our experimental system. While the geometrical differences may lead to local variations in flow behavior, the validated CFD framework was applied consistently. This distinction between validation and study configurations has now been clarified in the manuscript.

The simulations were conducted using a polyhexa core-type mesh, recognized for its efficiency and robustness. This type of mesh is particularly suitable for complex geometries, such as agitated vessels. During the grid independence test (cf. Fig. 5), several mesh sizes were tested for their impact on the computational results. Of these, M_5,

Table 4
Key geometrical dimensions of the impeller designs used in the experiments and simulations.

Impeller type	Disc diameter (mm)	Blade length (mm)	Blade width (mm)	Blade thickness (mm)	Blade angle	Number of blades	Notes
Rushton turbine	14.1	5.7	5.7	0.5	90°	6	Flat radial blades
Parabolic	14.1	4.1	Curved	0.48	Curved	6	Parabolic profile $y = 0.6x^2$
PBU	8.0	8.1	8.0	1.0	+45°	6	6 blades tilted upwards
PBD	8.0	8.1	8.0	1.0	−45°	6	6 blades tilted downwards

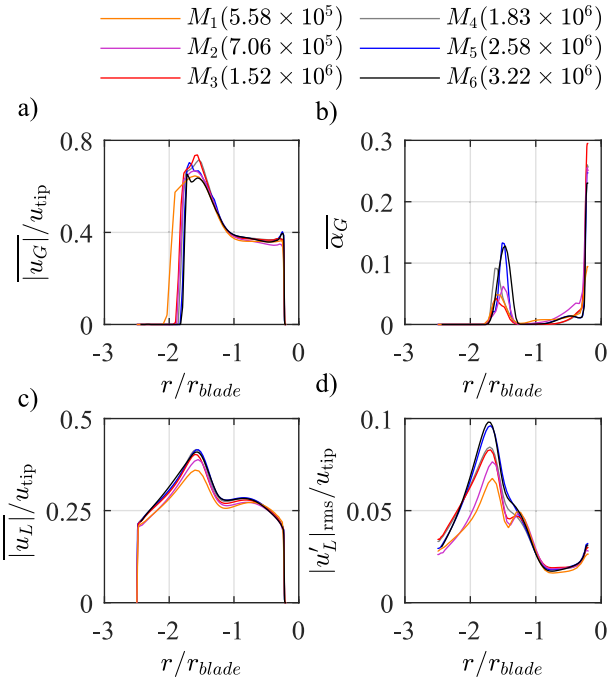

Fig. 5. Grid independence test results for a Rushton blade at ω_{blade} = 400 rpm, normalized by the blade tip velocity u_{tip} where applicable: (a) Time-averaged gas velocity magnitude $\overline{|u_G|}/u_{tip}$; (b) Time-averaged gas volume fraction $\overline{\alpha_G}$; (c) Time-averaged liquid velocity magnitude $\overline{|u_L|}/u_{tip}$; (d) RMS of liquid velocity magnitude fluctuations $|u'_L|_{rms}/u_{tip}$.

which corresponds to a mesh with 2.58×10^6 elements, was selected as the best choice for the URANS-Eulerian approach in two-phase flow modeling. This mesh configuration provides a good trade-off between computational cost and simulation quality. Although finer meshes like M_6 offer smoother flow fields, the gain in accuracy is minimal and is not justified by the increased computational effort. On the other hand, coarser meshes reduce the quality of captured flow features. For the DES modeling of the liquid phase, a finer mesh of 6.14×10^6 cells was used to ensure the resolution of the smaller flow structures inherent in the DES method.

4. Results and discussions

4.1. Experimental results: pH measurements and carbonation dynamics

Monitoring the pH drop in solutions, such as black liquor-NaOH, GLD-water, and ethanol-NaOH, offers an indispensable tool to understand and quantify carbonation [5,25,37,64]. Each of these solutions presents its own chemical intricacies due to their distinct compositions. For instance, black liquor-NaOH is rich in organic and inorganic substances from the pulp and paper process, while GLD-water has a mix of compounds that may influence its reactivity with CO_2. On the other hand, the ethanol-NaOH solution has its own set of reactions, especially when introducing CO_2. Despite these variances, the consistent theme is the observable drop in pH when CO_2 is introduced. This pH decrease directly relates to the formation of carbonate and bicarbonate species, indicative of the ongoing carbonation process. By monitoring this pH shift, one can infer the extent of carbonation, which is invaluable for process control, optimization, and ensuring the efficient utilization of CO_2 across different industrial contexts.

As shown in Fig. 6a, in the case of a mixture containing 5% w/v GLD in water, the performance of different impeller types for CO_2 absorption varies. Firstly, it is seen that stirring increases the rate at which the carbonation process is completed. The Rushton turbine proves to be the most effective, demonstrating its superior ability to promote CO_2 absorption in this specific mixture. These observations are in line with the numerical results, which show that the Rushton turbine has a more enhanced distribution of Q criterion, strain rate, and other relevant factors. However, it should be noted that the Rushton turbine also has the highest energy consumption among the four types, experiencing an approximate percentage increase of over 50% compared to the most energy-efficient option. Following closely in absorption performance is the PBU impeller, which also shows promising results in enhancing the absorption process. The Parabolic impeller ranks third, exhibiting moderate efficiency in CO_2 absorption and relatively lower energy consumption. Lastly, the PBD impeller performs the least effectively among the four types, indicating its limited suitability for this particular mixture despite its lower energy consumption. The enhanced performance of the Rushton turbine can be attributed to its ability to generate higher shear forces, but this comes at the expense of significantly higher energy consumption, making it a choice that involves trade-offs in this scenario.

It should be noted that the current discussion is based solely on experimental pH evolution. The hydrodynamic analysis from CFD simulations will be presented in the subsequent sections to complement these observations. As shown in Fig. 6b, for CO_2 absorption in GLD mixtures with 25% w/v solids, the Rushton turbine consistently outperforms other impellers. This performance reflects its capacity to generate high shear and maintain mixing even under challenging conditions with elevated solids content. In contrast, both the Pitch Blade Down-pumping (PBD) and Up-pumping (PBU) impellers show performance similar to the no-stirring case, suggesting that their lower shear does not sufficiently overcome the mixing limitations imposed by the high particle concentration. The Parabolic impeller performs slightly worse than the no-stirring case, which could be attributed to unfavorable flow patterns or the sparger's position creating recirculation zones that limit gas–liquid contact efficiency.

The difference between the behavior at 5% and 25% w/v GLD is primarily due to changes in the mixture's physical properties. At 5% GLD (Fig. 6a), the fluid remains relatively water-like, enabling impellers like PBD and PBU to provide effective mixing and facilitate CO_2 absorption. However, at 25%, the mixture becomes more viscous and may exhibit non-Newtonian characteristics, diminishing the effectiveness of low-shear impellers. This trend is also reflected in the black liquor results (Fig. 6c), where the Rushton turbine again demonstrates superior performance, while PBD and PBU are moderately effective, and the Parabolic impeller shows limited benefit compared to no stirring. These results underline that the performance of impeller designs is highly dependent on the fluid's rheology and solids content. The CFD-based hydrodynamic analysis, which further explains these experimental findings, will be presented in the following sections.

As shown in Fig. 6d, the performance of different impeller types for CO_2 absorption in ethanol with 2 g/L NaOH shows relatively minor

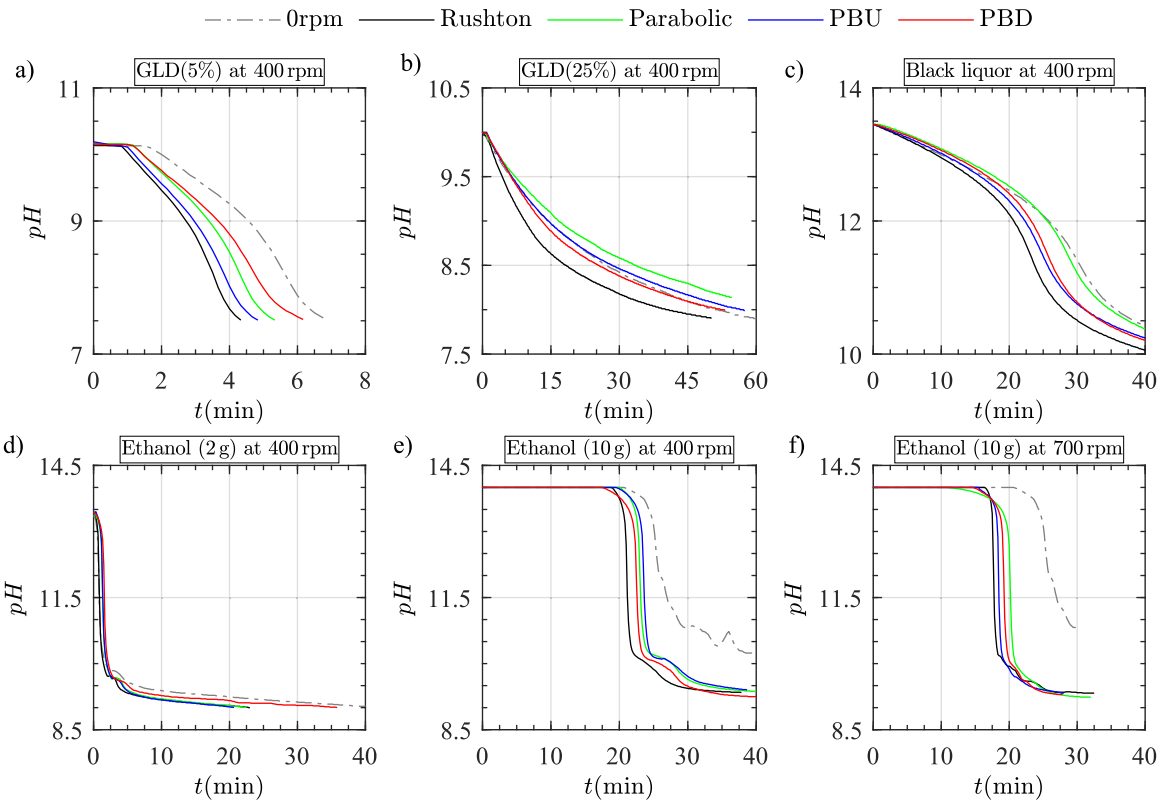

Fig. 6. Time series of pH curves for various solutions at different conditions: (a) Aqueous GLD (5% w/v) at ω_{blade} = 400 rpm; (b) Aqueous GLD (25% w/v) at ω_{blade} = 400 rpm; (c) Black liquor with 4% NaOH at ω_{blade} = 400 rpm; (d) Ethanol (2 g/L NaOH) at ω_{blade} = 400 rpm; (e) Ethanol (10 g/L NaOH) at ω_{blade} = 400 rpm; (f) Ethanol (10 g/L NaOH) at ω_{blade} = 700 rpm.

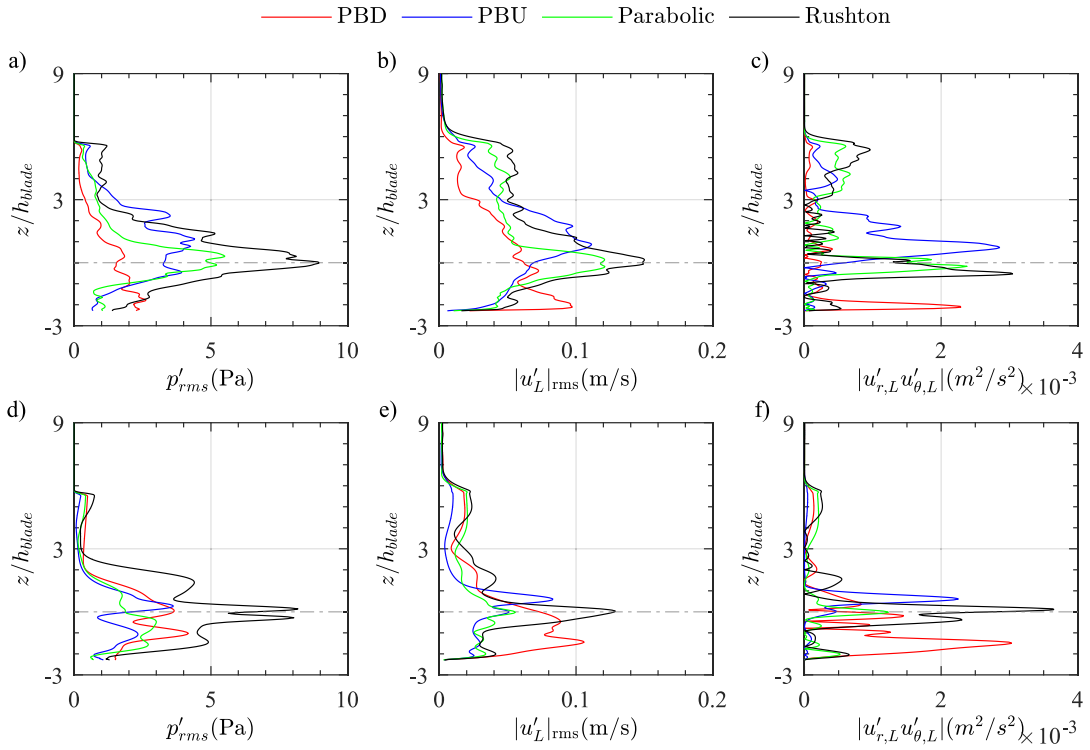

Fig. 7. Fluctuations sampled along a vertical line at r/r_{blade} = 1.4 in a fluid representing ethanol-NaOH for two viscosities. **First Row** (μ = 1.2 mPa s, ω_{blade} = 400 **rpm**): (a) RMS of static pressure p'_{rms} (Pa); (b) RMS velocity magnitude $\left|u'_L\right|_{\text{rms}}$ (m/s); (c) $u'_{r,L}u'_{\theta,L}$ stress (m^2/s^2). **Second Row** (μ = 20 mPa s, ω_{blade} = 700 **rpm**): (d) RMS of static pressure p'_{rms} (Pa); (e) RMS velocity magnitude $\left|u'_L\right|_{\text{rms}}$ (m/s); (f) $|u'_{r,L}u'_{\theta,L}|$ stress (m^2/s^2).

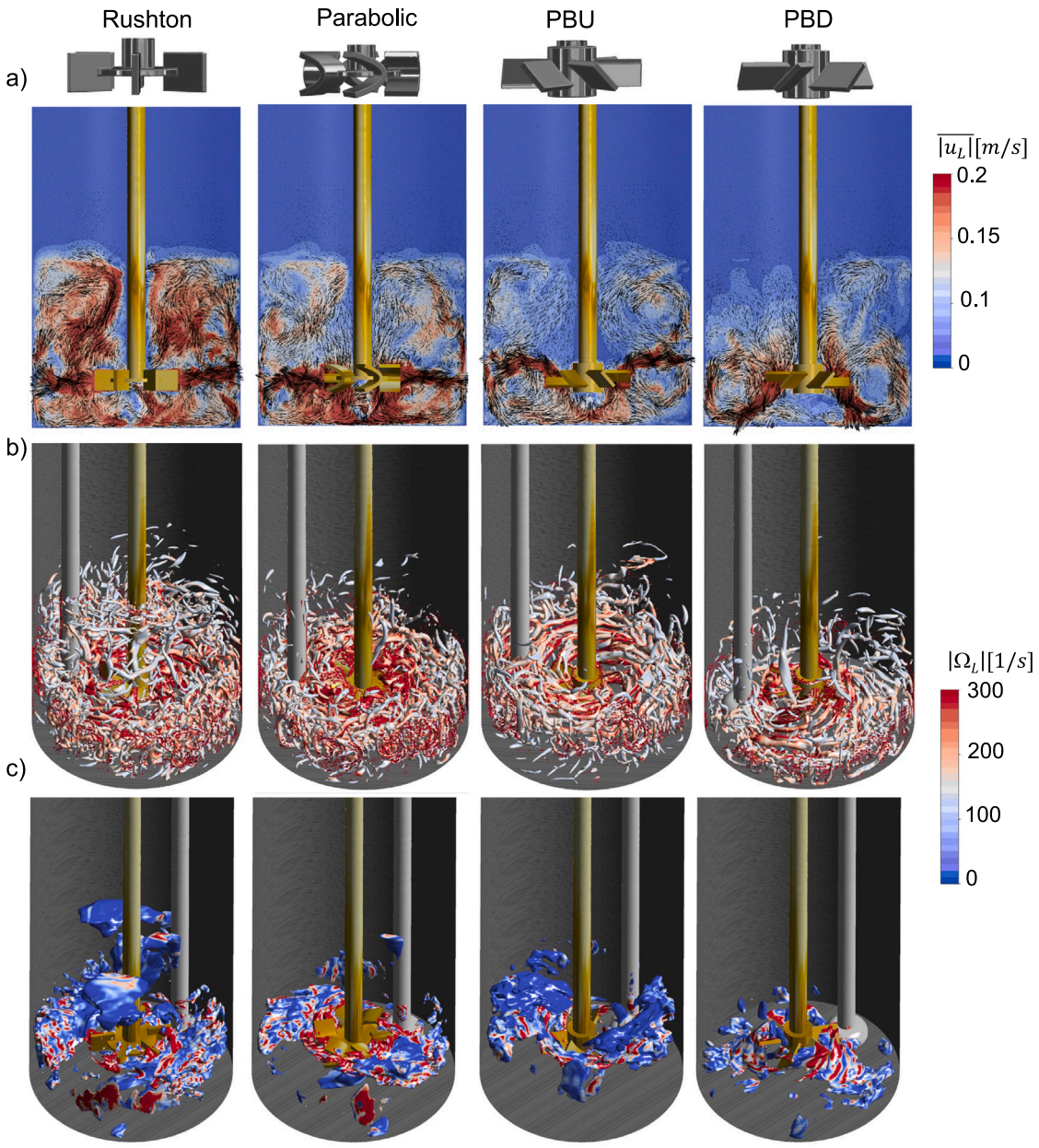

Fig. 8. For a fluid representing ethanol-NaOH viscosity (μ = 1.2 mPa s) at ω_{blade} = 400 rpm: (a) Velocity vectors for different impellers, colored by magnitude; (b) Q-criterion iso-surface for Q = 8000 s^{-2}, colored by vorticity; (c) Iso-surface of $u'_{r,L}u'_{\theta,L}$ stress with a value of 0.001 m^2/s^2, colored by vorticity.

variation. The Rushton, Parabolic, and PBU impellers exhibit similar behavior, with PBU showing slightly better performance, consistent with CFD predictions of favorable mixing. The PBD impeller, however, performs poorly, resembling the no-stirring case, which aligns with its weaker flow patterns seen in CFD. In this case, the pH decline occurs almost immediately after CO_2 introduction, reflecting rapid NaOH consumption under low-viscosity conditions.

In the case of ethanol with 10 g/L NaOH (Fig. 6e), where the mixture becomes highly viscous, the impeller performance shifts noticeably over time. Initially, Rushton performs best due to effective mixing at low viscosity. However, as carbonation progresses and viscosity increases, its performance declines. PBD becomes more effective in later stages, aided by its downward pumping, which supports mixing under high-viscosity conditions. PBU and Parabolic show intermediate performance throughout. Notably, in this case, the pH remains stable for an extended period before dropping sharply, indicating that the high NaOH concentration initially buffers the pH until sufficient CO_2 is absorbed to drive the reaction. This delayed pH response highlights how NaOH consumption is strongly linked to both concentration and mixing efficiency under varying viscosities.

This contrast between the 2 g/L and 10 g/L NaOH cases demonstrates that both impeller selection and solution properties influence carbonation dynamics. The pitch blade impeller, which can switch between PBD and PBU modes by reversing rotation, offers operational flexibility. In the early stages, PBU enhances mixing and gas–liquid mass transfer, reducing pH efficiently. As viscosity increases, switching to PBD supports continued mixing, allowing effective CO_2 absorption even under high-viscosity conditions.

As shown in Fig. 6f, in the case of ethanol with 2 g/L NaOH at 700 rpm, all impeller designs show satisfactory performance, considering the total process time of approximately 28 min. However, in the initial phase until time = 20 min, the Rushton turbine proves to be the most effective in promoting CO_2 absorption, followed by the PBU impeller. The PBD design ranks third, demonstrating its moderate efficiency, and

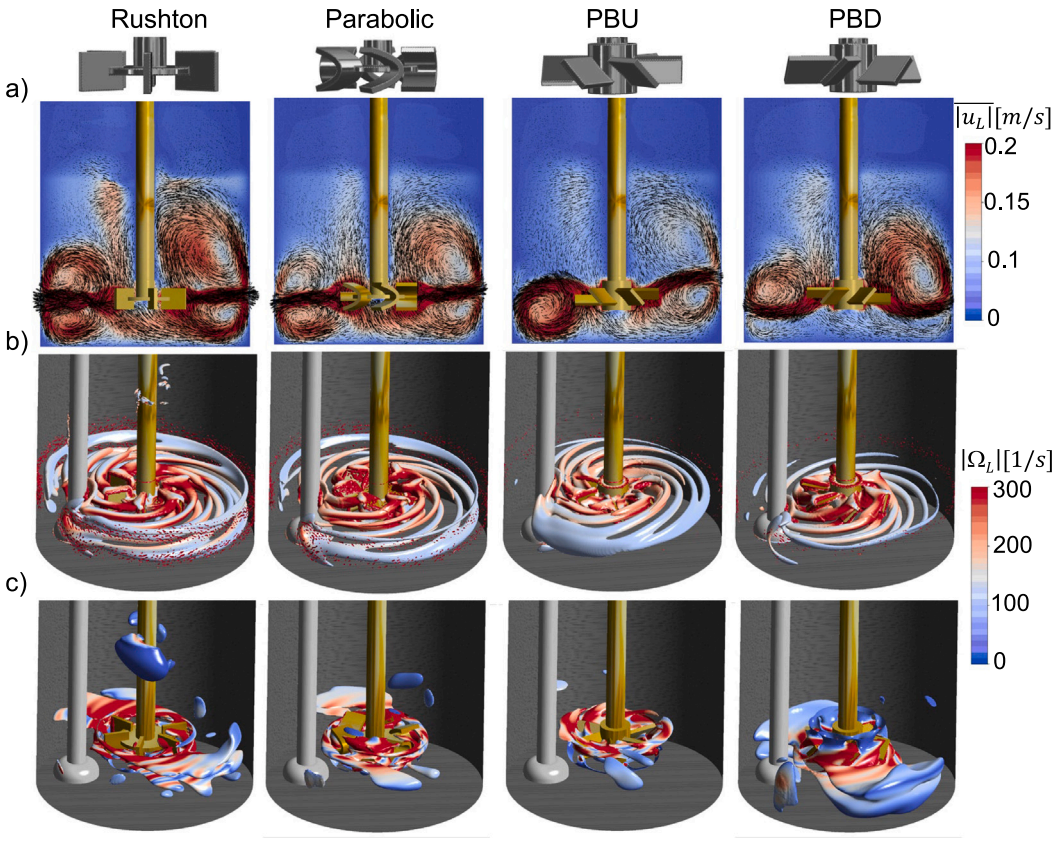

Fig. 9. For a fluid representing a highly viscous ethanol-NaOH solution (μ = 20 mPa s) at ω_{blade} = 700 rpm: (a) Velocity vectors for different impellers, colored by magnitude; (b) Q-criterion iso-surface with a value of Q = 5000 s^{-2}, colored by vorticity; (c) Iso-surface of $u'_{r,L}u'_{\theta,L}$ stress with a value of 0.001 m^2/s^2, colored by vorticity.

the Parabolic impeller performs least effectively during this period. As the process continues beyond 20 min, all impellers exhibit comparable performance, highlighting their adaptability to handling the changes in mixture properties over time. The overall process efficiency is notable, showcasing the potential of these impeller designs in achieving effective CO_2 absorption in the given ethanol-NaOH mixture under the specified operating conditions at 700 rpm. While the Rushton impeller demonstrates higher effectiveness in certain cases, it is important to consider other practical aspects, such as the required power. The Rushton impeller typically demands a significantly higher power compared to the PBU or PBD designs. As a result, PBU and PBD impellers can be more favorable options, offering a good balance between efficiency and energy consumption. The choice of the most suitable impeller should be based on a comprehensive evaluation of both performance and operational considerations to optimize the CO_2 absorption process effectively and economically.

4.2. Numerical results: Computational analysis of mixing dynamics

The study started from observations of a green liquid dregs (GLD) water solution with a concentration of 5% w/v, which closely mimics water in its properties. Our primary objective was to examine the impact of gas–liquid interactions in four distinct impeller designs and to discern their consequent effects on mixing characteristics. To establish a reliable baseline, CFD simulations were initially performed using water, commonly utilized as a benchmark in such studies, at a rotational speed of 400 rpm. The exploration then progressed to a low viscosity ethanol-NaOH solution (μ = 1.2 mPa s) under identical conditions to elucidate the nuanced effects of gas sparging on this medium. However, notable viscosity alterations in ethanol-NaOH postcarbonation necessitated additional analysis. To address this change, we simulated ethanol-NaOH whose viscosity was increased by a factor of 17 (cf. Table 2), maintaining rotation at 400 rpm. Recognizing the potential ramifications of elevated viscosity on mixing dynamics, further simulations were conducted at 700 rpm for the viscosity-enhanced ethanol-NaOH solution. Through an in-depth evaluation of these diverse scenarios, our research strives to provide exhaustive insights into the modulation of ethanol-NaOH by gas sparging under varying viscosities and rotational velocities, underscored by the role of disparate impeller designs in influencing mixing patterns.

4.2.1. Continuous phase mixing dynamics

Fig. 7 presents the performance of four distinct impeller blade designs: Rushton, parabolic, PBU, and PBD, in ethanol-NaOH for two different viscosities, sampled along a vertical axis at r/r_{blade} = 1.4. In the first row (μ = 1.2 mPa s and ω_{blade} = 400 rpm), the Rushton design stands out in all parameters: the RMS of static pressure fluctuation (Fig. 7a), the RMS of velocity magnitude fluctuation (Fig. 7b), and $u'_{r,L}u'_{\theta,L}$ stress (Fig. 7c). The Reynolds stress component $u'_{r,L}u'_{\theta,L}$ is crucial in evaluating impeller designs as it captures the interaction between radial and tangential turbulence intensities, directly influencing the mixing efficiency and flow structures in the tank. The PBU design follows the Rushton in performance, whereas the influence of the parabolic blade appears more localized, mainly concentrated near the blade in the range y/h_{blade} = −1 to 1. The second row, for μ = 20 mPa s at ω_{blade} = 700 rpm, again accentuates the Rushton's superior performance in the RMS of static pressure fluctuation (Fig. 7d), the RMS of velocity magnitude fluctuation (Fig. 7e), and $u'_{r,L}u'_{\theta,L}$ stress (Fig. 7f). In this scenario, the PBD design is the next most effective, followed by PBU, with the parabolic design's influence remaining localized. The results underscore the influence of blade design on mixing efficiency, especially under varied conditions of viscosity and rotational speed.

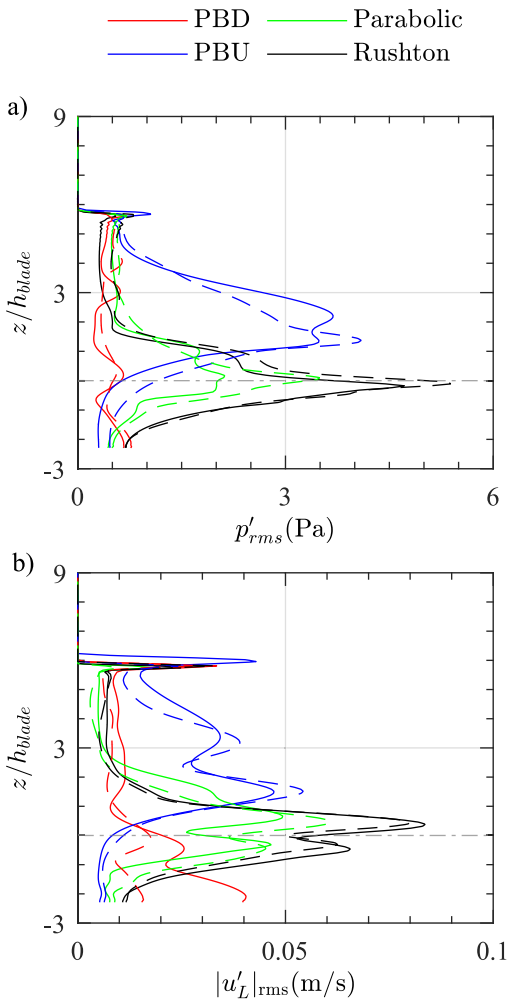

Fig. 10. (a) RMS of static pressure fluctuation, p'_{rms}; (b) RMS of modulus of velocity fluctuations, $\left|u'_L\right|_{\rm rms}$. Solid lines represent ethanol-NaOH (μ = 1.2 mPa s) and dashed lines indicate water. All data are taken at $\omega_{\rm blade}$ = 400 rpm at $r/r_{\rm blade}$ = 1.4. Impeller types are differentiated in the legend.

The observed correlation between p'_{rms}, $\left|u'_L\right|_{\rm rms}$, and $u'_{r,L}u'_{\theta,L}$ is intriguing, especially as pressure fluctuations are not typically a primary focus in stirred tank analyses. This suggests a unique coupling of momentum and pressure fields in the impeller-induced turbulence, warranting deeper exploration. In turbulent flows, especially in stirred tanks, the presence of vortices and eddies inherently causes fluctuations in both velocity and pressure fields. The momentum equation, which govern the fluid flow, couple velocity and pressure fields. In turbulent regions where Reynolds stress terms, such as $u'_{r,L}u'_{\theta,L}$, are significant, pressure fluctuations arise due to rapid adjustments accommodating velocity changes. The role of the impeller is to impart momentum, causing both velocity and pressure fluctuations, while the energy cascade in turbulence also links these fluctuations. In essence, the interplay between velocity and pressure in turbulent fluid dynamics and the impeller's role in generating turbulence explains this observed behavior.

Fig. 8a shows the velocity vector field superimposed on the velocity magnitude contour, providing a view of flow patterns and fluid velocities for different blade designs. The Rushton blade exhibits well-defined flow patterns with robust mixing characteristics, as evidenced by its pronounced and vigorous flow, followed by the PBU, while the Parabolic blade shows more localized and intensified flow near the blade. The PBU exhibits weaker and less dynamic flow patterns. The Q criterion is widely employed in fluid dynamics to identify vortex cores and evaluate turbulent structures in flows. In the context of our study, it serves as a critical metric for qualitatively assessing the efficiency and effectiveness of different impeller designs in mixing applications. The Q criterion is mathematically defined as $Q = \frac{1}{2}\left(\|\Omega\|^2 - \|S\|^2\right)$, where Ω and S denote the vorticity and strain-rate tensors, respectively. Fig. 8b presents the isosurface of the Q criterion, with color representation based on vorticity values. The Rushton blade exhibits the best performance with well-defined and widely spread vortical structures, corresponding to the highest volume-averaged vorticity value of 34.94 s^{-1}. The Parabolic blade shows the next highest vorticity value at 27.87 s^{-1}, but this is largely concentrated near the impeller region, with limited spatial dispersion. The PBU impeller, despite a slightly lower vorticity value of 24.23 s^{-1}, demonstrates a broader spread of vortical structures throughout the mixing volume, suggesting more effective bulk mixing. The PBD exhibits the weakest vortices and the lowest vorticity value at 21.15 s^{-1}. Fig. 8c depicts the iso-surface of $u'_{r,L}u'_{\theta,L}$ stress, valued at 0.001 m^2/s^2, with coloring based on vorticity. This presentation allows for the observation and analysis of fluctuations in the velocity components in the radial and tangential directions under different impeller operations. The depicted stresses are important indicators of the turbulence levels generated by the various impeller designs, providing insight into their respective mixing efficiencies. The patterns observed in this subfigure are consistent with those in Fig. 8b, with the Rushton blade and PBU showing better performance in generating turbulence, which is crucial for effective mixing.

Fig. 9 shows the mixing behavior of the different blade designs with increased liquid viscosity. The Rushton blade continues to stand out as the most effective, even with the higher viscosity. Its ability to generate well-defined and powerful vortices, despite the increased resistance to flow, highlights its robust mixing capabilities. Surprisingly, the Pitch blade down pumping (PBD) exhibits improved performance compared to the previous figure. The downward flow pattern leads to the formation of two large vortices in the upward direction, creating a unique mixing mechanism that enhances agitation and mixing, possibly due to the higher viscous forces aiding in vortex stabilization. On the other hand, the PBU experiences a reduction in flow patterns' strength. The vortices seem to struggle to form in the downward direction, likely due to the increased resistance from the higher viscosity, which hinders the mixing effectiveness of this blade design. For the Parabolic blade, the results remain least favorable, consistent with the previous case presented in Fig. 8. The Q criterion's reduced fragmentation into small parts suggests that the increased viscosity significantly limits the mixing potential of this blade design. These observations emphasize the impact of increased liquid viscosity on the mixing performance of the blade designs. While some designs, like Rushton and PBD, seem to benefit from higher viscosity by creating more stable and efficient vortices, others, like PBU and Parabolic, face challenges in maintaining their mixing effectiveness. These findings provide valuable subjective explanations for understanding the complex interactions between blade designs and fluid properties in a real-world carbonation scenario with increased liquid viscosity. As shown in Fig. 9c, at 700 RPM and higher viscosity, the PBD design continues to show enhanced mixing compared to PBU and Parabolic design. Interestingly, reversing the direction of rotation of the pitch blade after the liquid becomes viscous seems to improve mixing efficiency. The resolved $u'_{r,L}u'_{\theta,L}$ stress analysis confirms that the PBD and PBU blades generate stronger turbulent fluctuations and stress distribution in their respective favorable scenarios, leading to more efficient mixing and agitation. These findings shed light on the importance of considering both blade design and fluid properties to optimize mixing processes in real-world applications, particularly when dealing with variable viscosities and RPMs. In our simulations of the unbaffled tank, we carefully examined the free surface for any observable vortex formation. No prominent surface vortex was detected in the simulation results, likely due to the relatively low impeller rotational speeds used in our study, which may not have been sufficient to induce significant vortex formation. Additionally, the presence of

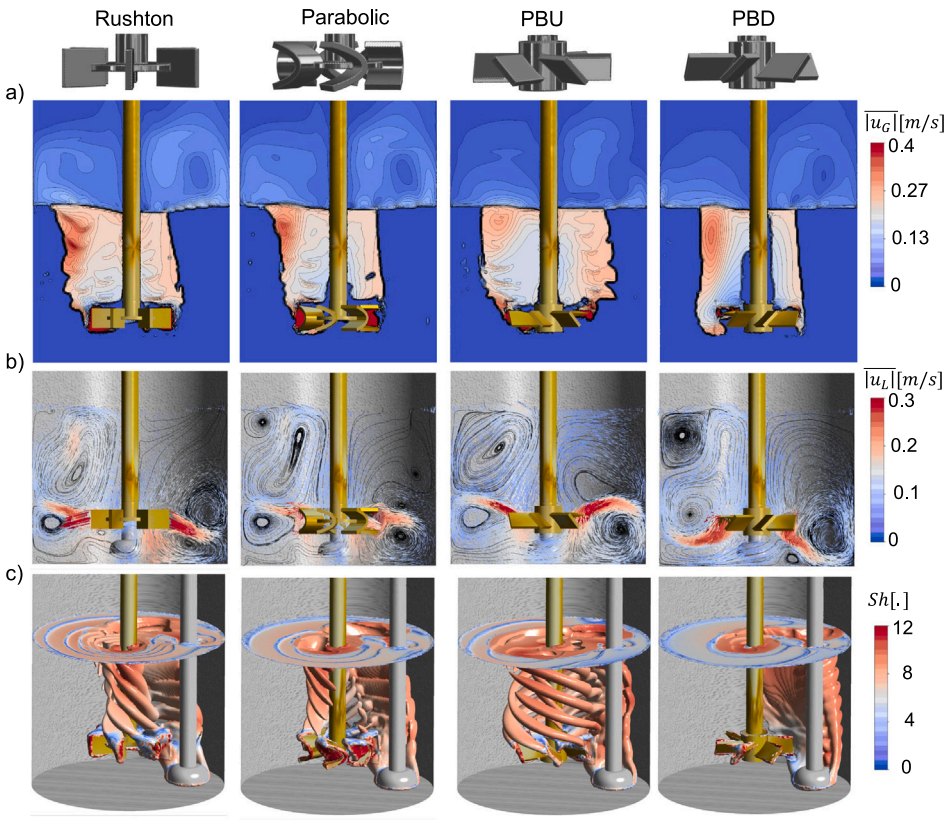

Fig. 11. At ω_{blade} = 400 rpm for Water (μ = 1.2 mPa s): (a) Contour of gas modulus of velocity; (b) Gas velocity vectors with streamlines superimposed; (c) Iso-surface of gas volume fraction $\alpha_G = 0.01$ colored by Sherwood number.

gas sparging may have disrupted any stable vortex structures from developing. While the absence of a strong surface vortex suggests minimal air entrainment, we acknowledge that in certain conditions with higher rotational speeds or varying liquid heights, such vortices could form and potentially influence the gas–liquid mixing process. Future studies may investigate this aspect in greater detail to assess its potential impact on carbonation dynamics.

4.2.2. Liquid-gas dispersion

In Fig. 10, results from a multiphase flow analysis within a mixing tank demonstrate the distinctive influences of various impeller designs on the flow parameters of two liquids: ethanol-NaOH (μ = 1.2 mPa s) and water. Fig. 10a shows the RMS of static pressure fluctuations, p'_{rms}, while Fig. 10b presents the RMS of the modulus of velocity fluctuations, $\left|u'_L\right|_{\text{rms}}$. The Rushton turbine emerges as the most efficient impeller, and the PBU design showcases commendable performance, subsequently trailed by the parabolic and PBD designs. Such consistent findings between single and multiphase flow scenarios underline the value of single-phase flow studies, implying that their insights remain pertinent even when introducing the complications of gas sparging.

In Fig. 11a, the contours of the gas modulus of velocity suggest a more uniform gas distribution for the Rushton and PBU designs, emphasizing their effective mixing capabilities. Fig. 11b with gas velocity vectors and superimposed streamlines offers insights into the internal flow dynamics, particularly emphasizing the pronounced upward and downward movements of the PBU and PBD impeller designs. In gas–liquid mixing processes, the Sherwood number Sh characterizes the efficiency of mass transfer at the gas–liquid interface. The bubble diameter, d_B, is the primary length scale, representing the immediate interface for transfer. The Schmidt number Sc is given by $Sc = \frac{\mu}{\rho D_{AB}}$,

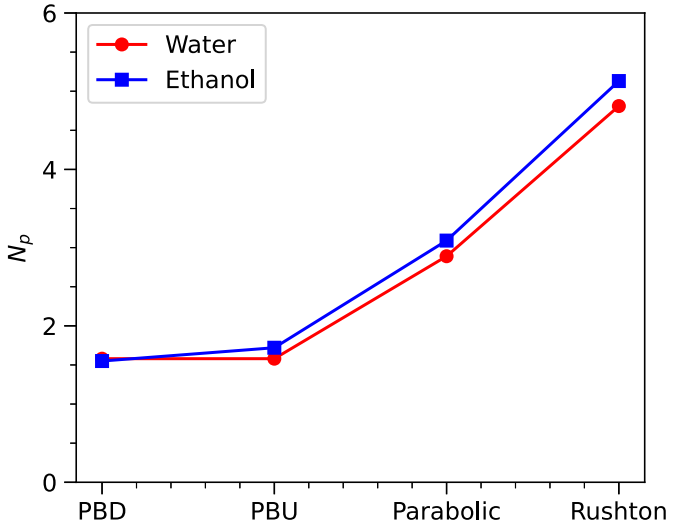

Fig. 12. Power number N_p for different impeller designs in water and ethanol-NaOH (μ = 1.2 mPa s) at ω_{blade} = 400 rpm.

where D_{AB} represents the diffusion coefficient of the dissolved species from the gas phase in the solution. The values of D_{AB} for CO_2 in water and CO_2 in ethanol are 1.98×10^{-9} m^2 s^{-1} and 4.89×10^{-9} m^2 s^{-1} respectively [65]. The design and operation of the impeller significantly influence the relative velocity, with various designs inducing different flow patterns, turbulence intensities, and shear rates. The relationship of Sh with the Reynolds and Schmidt numbers can be expressed as

$Sh = f(Re, Sc)$. One common Sherwood correlation is:

$$Sh = a \cdot Re^{b} \cdot Sc^{c} \tag{13}$$

where $a = 0.46$, $b = \frac{1}{2}$, and $c = \frac{1}{3}$ are the empirical constants [66]. Fig. 11c displays regions of efficient mass transfer, depicted by an iso-surface at $\alpha_G = 0.01$, colored by the Sherwood number Sh. Interestingly, the PBU configuration exhibits promising indications of efficiency in mass transfer, as suggested by the iso-surface contours. While the Rushton turbine is generally recognized for its superior performance, the visual data presented here offer valuable insights into the potential effectiveness of PBU as well, without making definitive comparative assertions. The omission of the ethanol-NaOH case with low viscosity in Fig. 11c is reasonable, given its mass transfer characteristics align closely with the water case, as depicted in Fig. 10.

The impeller performance was evaluated using the power number N_p, a dimensionless parameter widely used to characterize the mixing efficiency and energy consumption of stirred tanks, independent of reactor size and fluid properties. Reducing power consumption, as emphasized by Salho and Hamzah [67], is crucial as it directly translates to cost savings and enhances the mixing process. In our study, the torque required by each impeller design was calculated from CFD simulations, and subsequently, the power number was computed as:

$$N_p = \frac{P_{\text{req}}}{\rho N^3 d_{blade}^5} = \frac{2\pi \cdot N \cdot \text{Torque}}{\rho N^3 d_{blade}^5} \tag{14}$$

where P_{req} is the power (W), ρ the fluid density (kg/m^3), N the impeller rotational speed (rev/s), and d_{blade} the impeller diameter (m). The computed power number allows a direct and reliable comparison of impeller designs, aiding the selection of the most energy-efficient mixing configuration.

In Fig. 12, the power number N_p obtained from CFD simulations is shown for various impeller designs operating in water and ethanol-NaOH ($\mu = 1.2$ mPa s) at 400 rpm. The Rushton impeller consistently exhibits the highest power number in both fluids, aligning with results from [68], who demonstrated that Rushton-type impellers typically require more power compared to pitched blade impellers. Relative to the Rushton design in water, the PBD, PBU, and Parabolic designs demonstrate reductions in N_p of approximately 67.2%, 67.2%, and 39.9%, respectively. A similar trend is observed for the ethanol-NaOH solution, with the PBD, PBU, and Parabolic designs showing reductions of about 69.8%, 66.5%, and 39.8%, respectively. These power number values are consistent with previous experimental and numerical studies, confirming the reliability the present CFD methodology. Given its significantly lower power number and satisfactory mixing performance, the PBU impeller emerges as a promising energy-efficient alternative to the Rushton design. Such improvements in power consumption, as noted by Salho and Hamzah [67], are critical for reducing operational costs in industrial mixing applications. It is worth noting that while the power number is theoretically expected to remain constant in fully turbulent regimes, this condition is generally attained only at very high Reynolds numbers ($Re > 10^6$), which are typical of large-scale industrial reactors. In our small-scale system, the Reynolds numbers are one to two orders of magnitude lower, meaning that viscous effects remain significant and can cause N_p to vary with rotational speed and fluid properties, consistent with other experimental and numerical studies in similar regimes.

Fig. 13 depicts the fluctuation profiles in a fluid representing ethanol-NaOH with a viscosity of $\mu = 20$ mPa s at $\omega_{\text{blade}} = 700$ rpm. Fig. 13a presents the RMS of static pressure fluctuation, p'_{rms}, while Fig. 13b showcases the RMS of modulus of velocity fluctuation, $\left|u'_L\right|_{\text{rms}}$. At this heightened viscosity, the Rushton design maintains its consistent performance. Notably, the PBD impeller exhibits a strikingly better efficiency compared to the PBU in this context. Fig. 14 presents the contours of gas velocity for ethanol-NaOH with a viscosity of $\mu = 20$ mPa s under two varied impeller speeds. Specifically, in Fig. 14a corresponding to $\omega_{\text{blade}} = 400$ rpm, a discernible low-velocity zone is

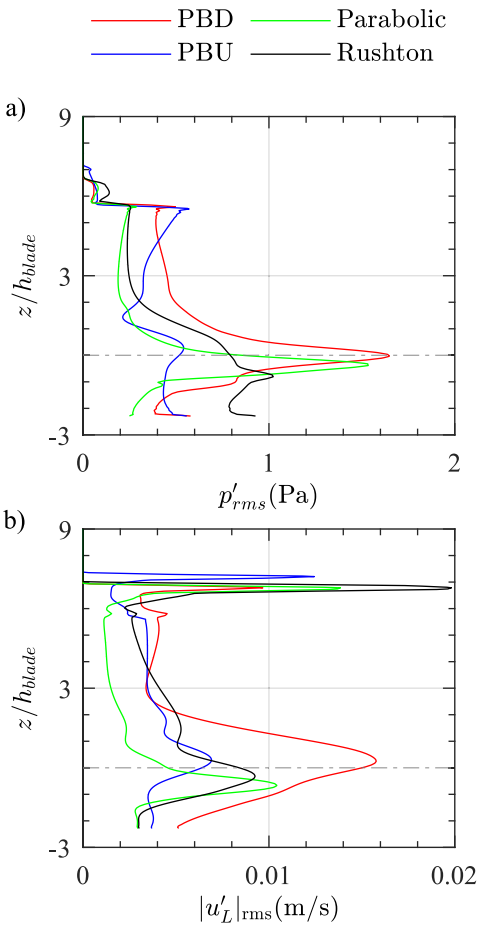

Fig. 13. Fluctuation profiles in a fluid representing a highly viscous ethanol-NaOH solution ($\mu = 20$ mPa s) at $\omega_{\text{blade}} = 700$ rpm at $r/r_{\text{blade}} = 1.4$: (a) RMS of static pressure fluctuation, p'_{rms}; (b) RMS of modulus of velocity fluctuation, $\left|u'_L\right|_{\text{rms}}$. The legend indicates the specific impeller designs.

evident at the center of the tank. This region of reduced flow activity becomes less pronounced at the heightened impeller speed of $\omega_{\text{blade}} = 700$ rpm, as illustrated in Fig. 14b. Across the impeller designs, the Rushton turbine consistently emerges as superior. Notably, in these more viscous conditions, the PBD design exhibits marked improvement over the PBU.

Fig. 15 illustrates iso-surfaces where the gas volume fraction is $\alpha_G = 0.01$, with these surfaces colored by the Sherwood number within an ethanol-NaOH medium of increased viscosity ($\mu = 20$ mPa s). Due to the increase in viscosity, the convective mass transfer decreases, resulting in lower Sherwood numbers. In Fig. 15a, at an impeller speed of $\omega_{\text{blade}} = 400$ rpm, there is a concentration of gas–liquid interaction close to the impeller, with the Sherwood number variations reflecting the efficacy of different impeller designs. The Rushton impeller yields satisfactory results, but intriguingly, the Pitch Blade Down (PBD) design surpasses the PBU at this speed. When the rotational speed is augmented to $\omega_{\text{blade}} = 700$ rpm in Fig. 15b, the distribution of gas volume fraction broadens, indicating improved mixing and larger mass transfer regions. The PBD shows its capability in facilitating gas dispersion in this more viscous environment, emerging as a valid consideration for efficient mass transfer tasks under such conditions.

Fig. 16 displays the power number N_p for various impeller designs in a high-viscosity ethanol-NaOH solution ($\mu = 20$ mPa s) at two rotational speeds. Notably, the power numbers at 400 rpm are consistently

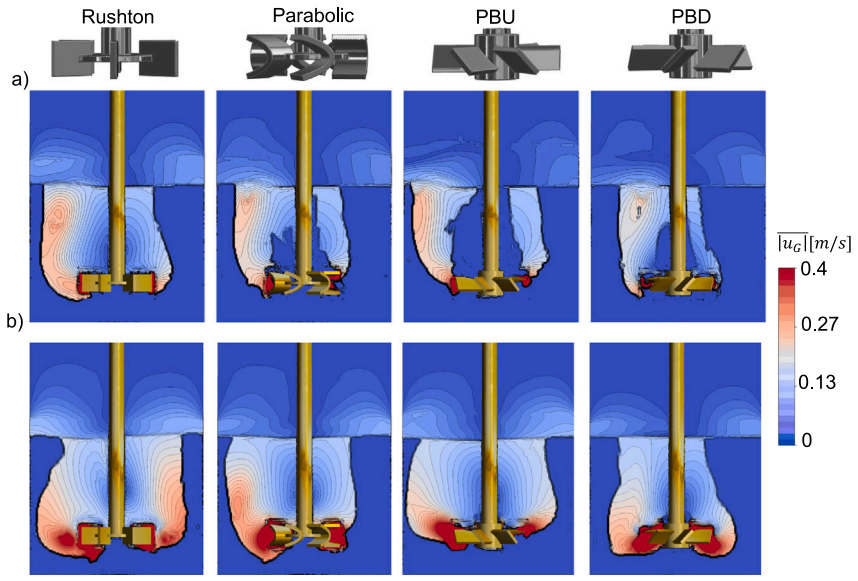

Fig. 14. Contours of gas velocity for a fluid representing a highly viscous ethanol-NaOH solution ($\mu = 20$ mPa s) at varied impeller speeds: (a) $\omega_{\text{blade}} = 400$ rpm; (b) $\omega_{\text{blade}} = 700$ rpm.

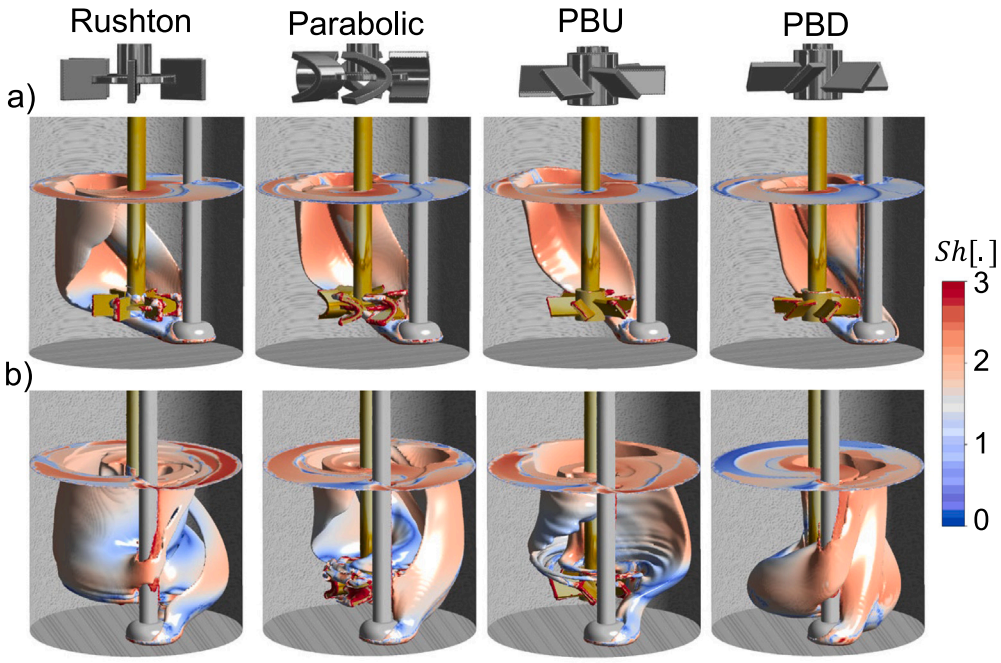

Fig. 15. Iso-surface of gas volume fraction $\alpha_G = 0.01$ colored by Sherwood number for a fluid representing a highly viscous ethanol-NaOH solution ($\mu = 20$ mPa s) at varying impeller speeds: (a) $\omega_{\text{blade}} = 400$ rpm; (b) $\omega_{\text{blade}} = 700$ rpm.

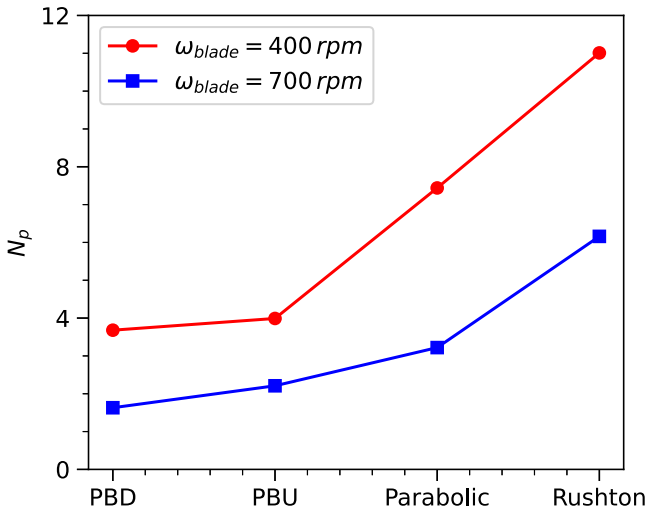

Fig. 16. Power number N_p for different impeller designs in a fluid representing high viscosity ethanol-NaOH solution (μ = 20 mPa s) at ω_{blade} = 400 rpm and ω_{blade} = 700 rpm.

higher than those at 700 rpm for all impeller designs, reflecting the reduced relative significance of viscous forces at the higher rotational speed. At ω_{blade} = 400 rpm, the Rushton impeller shows the highest power number, indicating the greatest energy requirement. Relative to the Rushton design, the PBD impeller achieves approximately 66.6% lower N_p, followed by the PBU and Parabolic impellers with reductions of about 63.8% and 32.4%, respectively. When increasing the rotational speed to ω_{blade} = 700 rpm, the difference between impellers becomes even more pronounced, with the PBD impeller demonstrating a reduction of about 73.5% in N_p compared to the Rushton impeller. These findings highlight the importance of impeller choice, especially in high-viscosity fluids, and indicate that higher rotational speeds generally improve the energy efficiency of mixing processes.

5. Conclusions

This study explored the impact of impeller design on the carbonation performance of CO_2-absorbing systems using real industrial by-products. A combination of experimental measurements and CFD simulations was used to evaluate four different impellers in various liquid systems, including NaOH in ethanol, black liquor, and green liquor dregs. These systems differ widely in viscosity, surface tension, and solid content, making them ideal for testing the sensitivity of carbonation performance to hydrodynamic conditions.

Our findings show that impeller performance is highly dependent on the physical and chemical characteristics of the absorbent. In low-viscosity solutions, such as diluted green liquor dregs or ethanol-NaOH at early carbonation stages, the Rushton turbine showed effective mixing and rapid CO_2 absorption, albeit with relatively high power demand. In contrast, for absorbents that become more viscous or contain solid particles, as in concentrated green liquor dregs or gel-forming NaOH-ethanol, pitch blade impellers — particularly in down-pumping mode — offered better performance and improved energy efficiency. For example, for aqueous green liquor dregs at ω_{blade} = 400 rpm, down-pumping mode operation of a pitch blade impeller exhibits 13% improved performance in reaching pH = 8.5 at 25% w/v, as opposed to a 23% advantage of the up-pumping mode at the more dilute 5% w/v condition. The capacity of the down-pumping mode to outperform the up-pumping mode when the solvent becomes more viscous is also confirmed for the ethanol-NaOH system, while demonstrating reductions in power number of up to 70% as compared to the Rusthon impeller. Another important outcome is the operational versatility of pitch blade impellers. Their ability to function in both up- and down-pumping modes enables process flexibility when the liquid properties change during carbonation. This adaptability is particularly valuable for systems where viscosity evolves over time, making a single impeller mode suboptimal throughout the entire process.

To our knowledge, this is one of the first studies combining both experimental carbonation data and CFD-based hydrodynamic analysis for CO_2 absorption using industrial alkaline residues. While the chemical reaction modeling is intentionally simplified in this study, the focus remains on understanding how fluid dynamics influence carbonation efficiency. These results suggest that impeller selection is not a one-size-fits-all decision but must be tailored to both the absorbent composition and its expected changes during operation. The study provides a useful reference for engineers and researchers involved in designing CO_2 capture processes using alkaline industrial residues. Further work can extend these findings by incorporating additional impeller types, evaluating continuous-flow conditions, or exploring scale-up effects.

CRediT authorship contribution statement

Abdul Raouf Tajik: Writing – original draft, Validation, Software, Methodology, Formal analysis, Conceptualization. **Emmanouela Leventaki:** Writing – review & editing, Validation, Methodology. **Francisco Baena-Moreno:** Writing – review & editing, Methodology. **Christian Kugge:** Resources, Methodology. **Diana Bernin:** Writing – review & editing, Supervision, Project administration, Funding acquisition, Conceptualization. **Henrik Ström:** Writing – review & editing, Supervision, Funding acquisition, Conceptualization. **Gaetano Sardina:** Writing – review & editing, Supervision, Funding acquisition, Conceptualization.

Declaration of competing interest

The authors declare the following financial interests/personal relationships which may be considered as potential competing interests: Diana Bernin reports financial support was provided by Swedish Energy Agency. If there are other authors, they declare that they have no known competing financial interests or personal relationships that could have appeared to influence the work reported in this paper.

Acknowledgments

The computations were enabled by resources provided by the National Academic Infrastructure for Supercomputing in Sweden (NAISS) at NSC partially funded by the Swedish Research Council through grant agreement no. 2022-06725. We acknowledge the Area of Advance Energy and Production, Chalmers University of Technology, and Energimyndigheten (P2021–00009) for financial support.

Appendix. Summary of governing equations

See Table 5.

Data availability

Data will be made available on request.

Table 5
List of governing equations used in the study.

Eq. no.	Equation	Description	Reference
A1	$\frac{\partial}{\partial t}\left(\alpha_k \rho_k\right) + \nabla \cdot \left(\alpha_k \rho_k \mathbf{u}_k\right) = 0$	Continuity equation for phase k	Prosperetti and Tryggvason [42]
A2	$\frac{\partial}{\partial t}\left(\alpha_k \rho_k \mathbf{u}_k\right) + \nabla \cdot \left(\alpha_k \rho_k \mathbf{u}_k \otimes \mathbf{u}_k\right) = -\alpha_k \nabla p + \nabla \cdot \left(\alpha_k (\boldsymbol{\tau}_k + \boldsymbol{\tau}_k^{Re})\right) + \mathbf{F}_k^{body} + \mathbf{F}_k^{inter}$	Momentum equation for phase k	Yeoh and Tu [43]
A3	$\mathbf{F}^{drag} = \frac{3}{4}\frac{C_D}{d_B}\alpha_G \rho_L \lvert\mathbf{u}_{rel}\rvert \mathbf{u}_{rel}$	Drag force term	Khopkar and Ranade [44]
A4	$Re_B = \frac{\lvert\mathbf{u}_{rel}\rvert d_B}{\nu_L}$	Bubble Reynolds number	Ishii and Zuber [48]
A5	$Eo = \frac{g\Delta\rho d_B^2}{\sigma}$	Eötvös number	Ishii and Zuber [48]
A6	$Mo = \frac{g\Delta\rho\rho_L^2 \nu_L^4}{\sigma^3}$	Morton number	Ishii and Zuber [48]
A7	$C_D = \max(C_{D,\text{sphere}}, \min(C_{D,\text{ellipse}}, C_{D,\text{cap}}))$	Ishii drag coefficient correlation	Ishii and Zuber [48]
A8	$\begin{cases} C_{D,\text{sphere}} = \frac{24}{Re}(1 + 0.15 Re_B^{0.75}) \\ C_{D,\text{ellipse}} = \frac{2}{3}\sqrt{Eo} \\ C_{D,\text{cap}} = \frac{8}{3} \end{cases}$	Sub-correlations for C_D	Tomiyama et al. [49]
A9	$\frac{\partial}{\partial t}\left(\alpha_L \rho_L k_L\right) + \nabla \cdot \left(\alpha_L \rho_L \mathbf{u}_L k_L\right) = \nabla \cdot \left(\alpha_L \left(\mu_L + \frac{\mu_{t,L}}{\sigma_k}\right)\nabla k_L\right) + \alpha_L \left(P_{k,c} - \rho_L \epsilon_L\right) + \alpha_L S_k^{BIT}$	Turbulent kinetic energy (TKE) equation	Jones and Launder [50]
A10	$\frac{\partial}{\partial t}\left(\alpha_L \rho_L \epsilon_L\right) + \nabla \cdot \left(\alpha_L \rho_L \mathbf{u}_L \epsilon_L\right) = \nabla \cdot \left(\alpha_L \left(\mu_L + \frac{\mu_{t,L}}{\sigma_\epsilon}\right)\nabla \epsilon_L\right) + \alpha_L \frac{\epsilon_L}{k_L}\left(C_{\epsilon,1} P_{k,c} - C_{\epsilon,2}\rho_L \epsilon_L\right) + \alpha_L S_\epsilon^{BIT}$	Turbulence dissipation rate equation	Jones and Launder [50]
A11	$S_k^{BIT} = C_k^{BIT} \mathbf{F}^{drag} \cdot \mathbf{u}_{rel}$	Source term for TKE due to bubble-induced turbulence	Troshko and Hassan [56]
A12	$S_\epsilon^{BIT} = C_\epsilon^{BIT} \frac{S_k^{BIT}}{\tau^{BIT}}, \quad \tau^{BIT} = \frac{d_B}{3 C_D \lvert\mathbf{u}_{rel}\rvert}$	Source term for dissipation due to BIT	Troshko and Hassan [56]
A13	$\frac{\partial(\rho k)}{\partial t} + \nabla \cdot (\rho \mathbf{u} k) = \nabla \cdot \left((\mu + \mu_t \sigma_k)\nabla k\right) + \tau_{ij} S_{ij} - \frac{\rho\sqrt{k^3}}{l_{RANS} \text{ or } l_{IDDES}}$	TKE transport (IDDES)	Shur et al. [60]
A14	$l_{RANS} = \frac{k^{1/2}}{\beta^* \omega}$	Turbulence length scale in RANS	Shur et al. [60]
A15	$l_{HYBRID} = \frac{k^{1/2}}{f_{\beta^*}\beta^* \tilde{\omega}}$	Hybrid turbulence length scale	Gritskevich et al. [61]
A16	$l_{IDDES} = f_d(1 + f_e) l_{RANS} + (1 - f_d) C_{DES} \Delta_{IDDES}$	IDDES length scale	Gritskevich et al. [61]
A17	$\Delta_{IDDES} = \min\left(\max(0.15 d_w, 0.15\Delta, \Delta_{\min}), \Delta\right)$	Grid scale for IDDES	Gritskevich et al. [61]

References

[1] T.I. Khan, A.R. Tajik, V. Parezanovic, Drag reduction of a generic transport vehicle model using a fluidic oscillator, Int. J. Thermofluids 15 (2022) 100180.

[2] K.S. Ng, N. Zhang, J. Sadhukhan, Techno-economic analysis of polygeneration systems with carbon capture and storage and CO2 reuse, Chem. Eng. J. 219 (2013) 96–108, http://dx.doi.org/10.1016/j.cej.2012.12.082.

[3] Y. Samarkin, M. Prodanovic, D. DiCarlo, A.R. Tajik, A. Wileman, Scco2 foams for geothermal reservoirs' stimulation: Impact of fracture roughness and temperature on rheology, in: SPE Annual Technical Conference and Exhibition?, SPE, 2024, D011S006R009.

[4] A.R. Tajik, A. Wileman, S. Wheeler, L. Morris, Y. Samarkin, M. Prodanovic, D. DiCarlo, Supercritical co2 foam stability and mobility for enhanced oil recovery and ccus: Experimental evaluation in simulated reservoir conditions, in: SPE/AAPG/SEG Carbon, Capture, Utilization, and Storage Conference and Exhibition, SPE, 2025, D021S021R001.

[5] F.M. Baena-Moreno, E. Leventaki, P.H. Ho, A.R. Tajik, D. Brzic, G. Sardina, H. Ström, D. Bernin, Potential of organic carbonates production for efficient carbon dioxide capture, transport and storage: reaction performance with sodium hydroxide–ethanol mixtures, Heliyon 9 (2023) e14140, http://dx.doi.org/10.1016/j.heliyon.2023.e14140.

[6] F.R. Siegel, Chapter 9 properties and uses of the carbonates, in: Developments in Sedimentology, Elsevier, 1967, pp. 343–393, http://dx.doi.org/10.1016/s0070-4571(08)71036-7.

[7] M. Tu, H. Zhao, Z. Lei, L. Wang, D. Chen, H. Yu, T. Qi, Aqueous carbonation of steel slag: A kinetics study, ISIJ Int. 55 (2015) 2509–2514, http://dx.doi.org/10.2355/isijinternational.isijint-2015-142.

[8] S.K. Kaliyavaradhan, T.C. Ling, Potential of CO 2 sequestration through construction and demolition (c & d) waste–an overview, J. CO2 Util. 20 (2017) 234–242, http://dx.doi.org/10.1016/j.jcou.2017.05.014.

[9] A.C. Spínola, C.T. Pinheiro, A.G. Ferreira, L.M. Gando-Ferreira, Mineral carbonation of a pulp and paper industry waste for CO2 sequestration, Process. Saf. Environ. Prot. 148 (2021) 968–979, http://dx.doi.org/10.1016/j.psep.2021.02.019.

[10] R. Sun, Y. Li, C. Liu, X. Xie, C. Lu, Utilization of lime mud from paper mill as CO2 sorbent in calcium looping process, Chem. Eng. J. 221 (2013) 124–132, http://dx.doi.org/10.1016/j.cej.2013.01.068.

[11] G. Pérez-López R. Montes-Hernandez, J. Nieto, F. Renard, L. Charlet, Carbonation of alkaline paper mill waste to reduce CO2 greenhouse gas emissions into the atmosphere, Appl. Geochem. 23 (2008) 2292–2300, http://dx.doi.org/10.1016/j.apgeochem.2008.04.016.

[12] F.M. Baena-Moreno, E. Leventaki, A. Riddell, J. Wojtasz-Mucha, D. Bernin, Effluents and residues from industrial sites for carbon dioxide capture: a review, Environ. Chem. Lett. 21 (2022) 319–337, http://dx.doi.org/10.1007/s10311-022-01513-x.

[13] G. Gadikota, K. Fricker, S.H. Jang, A.H.A. Park, Carbonation of silicate minerals and industrial wastes and their potential use as sustainable construction materials, in: ACS Symposium Series, American Chemical Society, 2015, pp. 295–322, http://dx.doi.org/10.1021/bk-2015-1194.ch012.

[14] W. Jonglertjunya, H.M. Tun, N. Khumphum, K. Charoenta, S. Chinkanjanarot, S. Srinives, N. Klomkliang, P. Phadungbut, Adsorption capability and regenerability of carbon slit micropores for co2 capture, Int. J. Thermofluids (2024) 100781, http://dx.doi.org/10.1016/j.ijft.2024.100781.

[15] J. Albertazzi, V. Busini, R. Rota, Comparison through a cfd approach of static mixers in an emulsification process, Int. J. Thermofluids (2024) 100708, http://dx.doi.org/10.1016/j.ijft.2024.100708.
[16] M. Guesmi, J. Manthey, R. Schab, S. Unz, M. Beckmann, Mechanistic modelling of water–oxygen bubbly flow in horizontal pipes: Deviation analysis from experimental correlations and performance comparison with cfd, Int. J. Thermofluids (2024) 101016, http://dx.doi.org/10.1016/j.ijft.2024.101016.
[17] A. Salama, S.E.D. El-Morshedy, Investigation of the steady state subcooled boiling regime in the hot subchannel of a vver-1200 reactor core: A cfd analysis, Int. J. Thermofluids (2024) 100947, http://dx.doi.org/10.1016/j.ijft.2024.100947.
[18] D. Adanta, D.P. Sari, I. Syofii, I. Thamrin, I. Yani, A.Marwani. Fudholi, A.P. Prakoso, Configuration blade shape for enhancement crossflow turbine performance by the cfd method, Int. J. Thermofluids (2024) 100665, http://dx.doi.org/10.1016/j.ijft.2024.100665.
[19] M. Laakkonen, P. Moilanen, J. Aittamaa, Local bubble size distributions in agitated vessels, Chem. Eng. J. 106 (2005) 133–143, http://dx.doi.org/10.1016/j.cej.2004.11.010.
[20] H.V. Hristov, B. Stephan, H. Uwe, K. Holger, H. Günther, S. Wilfried, A study on the two-phase flow in a stirred tank reactor agitated by a gas-inducing turbine, Chem. Eng. Res. Des. 86 (2008) 75–81, http://dx.doi.org/10.1016/j.cherd.2007.10.008.
[21] V. Ranade, M. Perrard, C. Xuereb, N.L. Sauze, J. Bertrand, Influence of gas flow rate on the structure of trailing vortices of a rushton turbine: PIV measurements and CFD simulations, Chem. Eng. Res. Des. 79 (2001) 957–964, http://dx.doi.org/10.1205/02638760152721190.
[22] G. Montante, A. Paglianti, Gas hold-up distribution and mixing time in gas–liquid stirred tanks, Chem. Eng. J. 279 (2015) 648–658, http://dx.doi.org/10.1016/j.cej.2015.05.058.
[23] P. Bajpai, Pulping fundamentals, in: Biermann's Handbook of Pulp and Paper, Elsevier, 2018, pp. 295–351, http://dx.doi.org/10.1016/b978-0-12-814240-0.00012-4.
[24] M.A. Azeez, Pulping of non-woody biomass, in: Pulp and Paper Processing, InTech, 2018, http://dx.doi.org/10.5772/intechopen.79749.
[25] M. Yoo, S.J. Han, J.H. Wee, Carbon dioxide capture capacity of sodium hydroxide aqueous solution, J. Environ. Manag. 114 (2013) 512–519, http://dx.doi.org/10.1016/j.jenvman.2012.10.061.
[26] T. Kinnarinen, M. Golmaei, E. Jernström, A. Häkkinen, Separation, treatment and utilization of inorganic residues of chemical pulp mills, J. Clean. Prod. 133 (2016) 953–964, http://dx.doi.org/10.1016/j.jclepro.2016.06.024.
[27] M.E. Eugenio, D. Ibarra, R. Martín-Sampedro, E. Espinosa, I. Bascón, A. Rodríguez, Alternative raw materials for pulp and paper production in the concept of a lignocellulosic biorefinery, in: Cellulose, IntechOpen, 2019, http://dx.doi.org/10.5772/intechopen.90041.
[28] V.R. dos Santos, M.D. Cabrelon, E. de Sousa Trichês, Green liquor dregs and slaker grits residues characterization of a pulp and paper mill for future application on ceramic products, J. Clean. Prod. 240 (2019) 118220, http://dx.doi.org/10.1016/j.jclepro.2019.118220.
[29] C. Nigéus, J. Lindblom, Hydrogeological properties of till amended with green liquor dregs (GLD): Recycling of an industrial residue for reclamation of acid generating mine sites, Geotech. Geol. Eng. 41 (2023) 3625–3639, http://dx.doi.org/10.1007/s10706-023-02477-7.
[30] M. Mäkitalo, J. Lu, C. Maurice, B. Öhlander, Prediction of the long-term performance of green liquor dregs as a sealing layer to prevent the formation of acid mine drainage, J. Environ. Chem. Eng. 4 (2016) 2121–2127, http://dx.doi.org/10.1016/j.jece.2015.10.005.
[31] E. Queiroz, E. Leventaki, C. Kugge, D. Bernin, Co2 capture through aqueous carbonation using green liquor dregs as the absorbent, ACS Sustain. Resour. Manag. 2 (2024) 119–126.
[32] Z.shan. Li, F. Fang, X.yu. Tang, N.sheng. Cai, Effect of temperature on the carbonation reaction of CaO with CO2, Energy Fuels 26 (2012) 2473–2482, http://dx.doi.org/10.1021/ef201543n.
[33] Y. Yoo, I. Kim, D. Lee, W.Y. Choi, J. Choi, K. Jang, J. Park, D. Kang, Review of contemporary research on inorganic CO2 utilization via CO2 conversion into metal carbonate-based materials, J. Ind. Eng. Chem. 116 (2022) 60–74, http://dx.doi.org/10.1016/j.jiec.2022.09.007.
[34] S.J. Han, J.H. Wee, Carbon dioxide fixation via the synthesis of sodium ethyl carbonate in NaOH-dissolved ethanol, Ind. Eng. Chem. Res. 55 (2016) 12111–12118, http://dx.doi.org/10.1021/acs.iecr.6b03250.
[35] J. Pak, S.J. Han, J.H. Wee, Precipitation of potassium-based carbonates for carbon dioxide fixation via the carbonation and re-carbonation of KOH dissolved aqueous ethanol solutions, Chem. Eng. J. 427 (2022) 131669, http://dx.doi.org/10.1016/j.cej.2021.131669.
[36] S.J. Han, J.H. Wee, Carbon dioxide fixation by combined method of physical absorption and carbonation in NaOH-dissolved methanol, Energy Fuels 31 (2017) 1747–1755, http://dx.doi.org/10.1021/acs.energyfuels.6b02709.
[37] E. Leventaki, F.M. Baena-Moreno, J. Wojtasz-Mucha, N. Sjöstedt, A.R. Tajik, G. Sardina, H. Ström, D. Bernin, Experimental evaluation of black liquor carbonation for carbon dioxide capture, J. CO2 Util. 72 (2023) 102516, http://dx.doi.org/10.1016/j.jcou.2023.102516.
[38] A.R. Tajik, T.I. Khan, V. Parezanović, Raster angle impact on fdm-based additive manufactured fluidic oscillator, Int. J. Thermofluids 16 (2022) 100230.
[39] A.R. Tajik, V. Parezanović, Additive manufacturing impact on a fluidic oscillator with respect to surface roughness, Int. J. Heat Fluid Flow 97 (2022) 109040.
[40] V. Radtke, D. Stoica, I. Leito, F. Camões, I. Krossing, B. Anes, M. Roziková, L. Deleebeeck, S. Veltzé, T. Näykki, F. Bastkowski, A. Heering, R. Dániel, L. Liv, E. Uysal, N. Lawrence, A unified pH scale for all solvents: part i – intention and reasoning (IUPAC technical report), Pure Appl. Chem. 93 (2021) 1049–1060, http://dx.doi.org/10.1515/pac-2019-0504.
[41] A. Gonçalves F. Trindade, C. Costa, J. Bernardo, I. Johnson, I. Fonseca, A. Ferreira, Pvt, viscosity, and surface tension of ethanol: New measurements and literature data evaluation, J. Chem. Thermodyn. 42 (2010) 1039–1049.
[42] A. Prosperetti, G. Tryggvason (Eds.), Computational Methods for Multiphase Flow, Cambridge University Press, 2007, http://dx.doi.org/10.1017/cbo9780511607486.
[43] G.H. Yeoh, J. Tu (Eds.), Computational Techniques for Multiphase Flows, Elsevier, 2010, http://dx.doi.org/10.1016/c2009-0-16604-7.
[44] A.R. Khopkar, V.V. Ranade, CFD simulation of gas–iquid stirred vessel: VC, s33, and l33 flow regimes, AIChE J. 52 (2006) 1654–1672, http://dx.doi.org/10.1002/aic.10762.
[45] F. Scargiali, A. D'Orazio, F. Grisafi, A. Brucato, Modelling and simulation of gas–liquid hydrodynamics in mechanically stirred tanks, Chem. Eng. Res. Des. 85 (2007) 637–646, http://dx.doi.org/10.1205/cherd06243.
[46] Q. Zhang, Y. Yong, Z.S. Mao, C. Yang, C. Zhao, Experimental determination and numerical simulation of mixing time in a gas–liquid stirred tank, Chem. Eng. Sci. 64 (2009) 2926–2933, http://dx.doi.org/10.1016/j.ces.2009.03.030.
[47] X. Guan, X. Li, N. Yang, M. Liu, CFD simulation of gas-liquid flow in stirred tanks: Effect of drag models, Chem. Eng. J. 386 (2020) 121554, http://dx.doi.org/10.1016/j.cej.2019.04.134.
[48] M. Ishii, N. Zuber, Drag coefficient and relative velocity in bubbly, droplet or particulate flows, AIChE J. 25 (1979) 843–855, http://dx.doi.org/10.1002/aic.690250513.
[49] A. Tomiyama, I. Kataoka, I. Zun, T. Sakaguchi, Drag coefficients of single bubbles under normal and micro gravity conditions, JSME Int. J. Ser. B 41 (1998) 472–479, http://dx.doi.org/10.1299/jsmeb.41.472.
[50] W. Jones, B. Launder, The prediction of laminarization with a two-equation model of turbulence, Int. J. Heat Mass Transfer 15 (1972) 301–314, http://dx.doi.org/10.1016/0017-9310(72)90076-2.
[51] M. Ciofalo, A. Brucato, F. Grisafi, N. Torraca, Turbulent flow in closed and free-surface unbaffled tanks stirred by radial impellers, Chem. Eng. Sci. 51 (1996) 3557–3573.
[52] A. Tamburini, A. Brucato, M. Ciofalo, G. Gagliano, G. Micale, F. Scargiali, Cfd simulations of early-to fully-turbulent conditions in unbaffled and baffled vessels stirred by a rushton turbine, Chem. Eng. Res. Des. 171 (2021) 36–47.
[53] G. Montante, A. Paglianti, F. Magelli, Experimental analysis and computational modelling of gas–liquid stirred vessels, Chem. Eng. Res. Des. 85 (2007) 647–653, http://dx.doi.org/10.1205/cherd06141.
[54] P. Shi, R. Rzehak, Bubbly flow in stirred tanks: Euler-euler/RANS modeling, Chem. Eng. Sci. 190 (2018) 419–435, http://dx.doi.org/10.1016/j.ces.2018.06.001.
[55] J. Li, B. Deng, B. Zhang, X. Shen, C.N. Kim, Cfd simulation of an unbaffled stirred tank reactor driven by a magnetic rod: assessment of turbulence models, Water Sci. Technol. 72 (2015) 1308–1318.
[56] A. Troshko, Y. Hassan, A two-equation turbulence model of turbulent bubbly flows, Int. J. Multiph. Flow 27 (2001) 1965–2000, http://dx.doi.org/10.1016/s0301-9322(01)00043-x.
[57] I. Kataoka, D. Besnard, A. Serizawa, Basic equation of turbulence and modeling of interfacial transfer terms in gas-liquid two-phase flow, Chem. Eng. Commun. 118 (1992) 221–236, http://dx.doi.org/10.1080/00986449208936095.
[58] K. He, G. Minelli, J. Wang, G. Gao, S. Krajnović, Assessment of LES, IDDES and RANS approaches for prediction of wakes behind notchback road vehicles, J. Wind Eng. Ind. Aerodyn. 217 (2021) 104737, http://dx.doi.org/10.1016/j.jweia.2021.104737.
[59] G. Chen, X.B. Li, X.F. Liang, IDDES simulation of the performance and wake dynamics of the wind turbines under different turbulent inflow conditions, Energy 238 (2022) 121772, http://dx.doi.org/10.1016/j.energy.2021.121772.
[60] M.L. Shur, P.R. Spalart, M.K. Strelets, A.K. Travin, A hybrid RANS-LES approach with delayed-DES and wall-modelled LES capabilities, Int. J. Heat Fluid Flow 29 (2008) 1638–1649, http://dx.doi.org/10.1016/j.ijheatfluidflow.2008.07.001.
[61] M.S. Gritskevich, A.V. Garbaruk, J. Schütze, F.R. Menter, Development of DDES and IDDES formulations for the k-ω shear stress transport model, Flow Turbul. Combust. 88 (2011) 431–449, http://dx.doi.org/10.1007/s10494-011-9378-4.
[62] N. Kazakis, A. Mouza, S. Paras, Experimental study of bubble formation at metal porous spargers: Effect of liquid properties and sparger characteristics on the initial bubble size distribution, Chem. Eng. J. 137 (2008) 265–281, http://dx.doi.org/10.1016/j.cej.2007.04.040.
[63] G. Montante, D. Horn, A. Paglianti, Gas–liquid flow and bubble size distribution in stirred tanks, Chem. Eng. Sci. 63 (2008) 2107–2118, http://dx.doi.org/10.1016/j.ces.2008.01.005.

[64] S.J. Han, M. Yoo, D.W. Kim, J.H. Wee, Carbon dioxide capture using calcium hydroxide aqueous solution as the absorbent, Energy Fuels 25 (2011) 3825–3834, http://dx.doi.org/10.1021/ef200415p.

[65] E.D. Snijder, M.J.M. te Riele, G.F. Versteeg, W.P.M. van Swaaij, Diffusion coefficients of CO, CO2, n2o, and n2 in ethanol and toluene, J. Chem. Eng. Data 40 (1995) 37–39, http://dx.doi.org/10.1021/je00017a010.

[66] D. Deising, D. Bothe, H. Marschall, Direct numerical simulation of mass transfer in bubbly flows, Comput. & Fluids 172 (2018) 524–537, http://dx.doi.org/10.1016/j.compfluid.2018.03.041.

[67] A.K. Salho, D.A. Hamzah, A review of stirred tank dynamics: Power consumption, mixing time and impeller geometry, Int. J. Heat Technol. (2024) 42.

[68] D. Cheng, J. Cheng, X. Li, X. Wang, C. Yang, Z.S. Mao, Experimental study on gas–liquid–liquid macro-mixing in a stirred tank, Chem. Eng. Sci. 75 (2012) 256–266.